Scientific Reports

https://doi.org/10.1038/s41598-026-35956-x

Article in Press

Visible-light photocatalytic mineralization of 4-Chlorophenol over ZnO-loaded sulfonated carbonaceous bentonite: kinetic analysis, pathway elucidation, and catalyst reusability

Received: 1 September 2025

Accepted: 9 January 2026

Published online: 16 January 2026

Cite this article as: Ahmed Z.M., Allam A.A., El-Sayed M.I. *et al.* Visible-light photocatalytic mineralization of 4-Chlorophenol over ZnO-loaded sulfonated carbonaceous bentonite: kinetic analysis, pathway elucidation, and catalyst reusability. *Sci Rep* (2026). https://doi.org/10.1038/s41598-026-35956-x

Zeinab M. Ahmed, Ahmed A. Allam, Mohamed I. El-Sayed, Ibrahim Mohamed Abd El-Gaied, Yasser Salama, Hassan A. Rudayni, Wail Al Zoubi & Mostafa R. Abukhadra

Visible-light photocatalytic mineralization of 4-Chlorophenol over ZnO-loaded sulfonated carbonaceous bentonite: Kinetic analysis, pathway elucidation, and catalyst reusability

Zeinab M. Ahmed[1]; Ahmed A. Allam[2]; Mohamed I. El-Sayed[1]; Ibrahim Mohamed Abd El-Gaied[1]; Yasser Salama[1]; Hassan A. Rudayni[2]; Wail Al Zoubi[3]; Mostafa R. Abukhadra[4]⋆

[1]Geology Department, Faculty of Science, Beni-Suef University, Beni-Suef, 65211, Egypt
[2]Department of Biology, College of Science, Imam Mohammad Ibn Saud Islamic University (IMSIU), Riyadh 11623, Saudi Arabia.
[3]*Materials Electrochemistry Laboratory, School of Materials Science and Engineering, Yeungnam University, Gyeongsan 38541, Republic of Korea*
[4]Geosciences Department, College of Science, United Arab Emirates University, 15551, Al Ain, United Arab Emirates.
Corresponding author⋆.Tel: +2001288447189. E-mail: m.abdelwahab@uaeu.ac.ae

Abstract

4-Chlorophenol (4-CL) is a toxic and persistent industrial pollutant resistant to conventional treatment, making its removal from wastewater a major environmental challenge. Visible-light photocatalysis provides a clean and efficient route for its complete mineralization. This study introduces a novel ZnO-functionalized sulfonated carbonaceous bentonite (ZnO@SB) nanohybrid, designed to enhance visible-light absorption, charge separation, and surface reactivity. The composite was synthesized via controlled sulfonation of organic-rich bentonite followed by uniform ZnO nanoparticle deposition. Structural and spectroscopic analyses confirmed successful functionalization and high ZnO dispersion across the sulfonated matrix. Under visible light, ZnO@SB (0.5 g/L, pH 8) achieved 100% degradation of 4-CL (5 mg/L) in 30 min and 100% TOC removal in 60 min (complete mineralization), following pseudo-first-order kinetics (k_1 = 0.1657 min^{-1}, R^2 > 0.98). The quantum yield increased from 7.39 × 10^{-8} to 2.96 × 10^{-7} with higher catalyst loading. The photocatalyst retained >90% activity after five cycles, with Zn^{2+} leaching below 0.005 mg/L, indicating excellent chemical stability. Mechanistic studies confirmed the dominant roles of superoxide ($O_2^{\bullet-}$) and hydroxyl (•OH) radicals in driving hydroxylation, dechlorination, and aromatic ring cleavage. The novelty of this work lies in the synergistic integration of sulfonated carbonaceous bentonite with ZnO, which simultaneously enhances adsorption, charge transfer, and visible-light response. This multifunctional hybrid provides a low-cost, stable, and highly efficient photocatalyst for scalable visible-light-driven degradation and mineralization of chlorinated phenolic pollutants.

Keywords: *4-Chlorophenol; ZnO@SB; Bentonite; Sulfonation; Visible-light photocatalysis; Wastewater treatment*

Introduction

The relentless expansion of industrial activities and human advancement has led to a substantial increase in the discharge of hazardous chemical pollutants into natural ecosystems. This ongoing contamination is exerting detrimental effects on aquatic environments, public health, and ecological stability on a global scale [1]. Among the various toxic substances released into water bodies, phenolic compounds are particularly notorious due to their severe toxicity. They are frequently introduced into the environment as residuals from the use of herbicides, petroleum-based chemicals, and wood-processing industries [2]. Chlorophenols, a significant subclass of phenolic pollutants, are commonly integrated into the synthesis of numerous chemical products, including fungicides and pesticides [2, 3]. These compounds pose serious environmental and health hazards even at very low concentrations. Their persistence in the environment, resistance to natural degradation, and tendency to bioaccumulate make them particularly alarming in terms of long-term ecological and toxicological impact [4, 5].

Scientific findings have consistently demonstrated that chlorophenols exhibit mutagenic, genotoxic, and carcinogenic characteristics. Their resistance to biological breakdown further enhances their environmental longevity, contributing to their widespread toxicity in both aquatic and terrestrial systems [2, 3, 6]. One of the most commonly used chlorophenols is 4-chlorophenol (4-CL), a compound employed extensively across several industries, including pharmaceuticals, petrochemicals, dyes, and general chemical manufacturing [7]. Due to its environmental stability, toxic nature, and carcinogenic potential, 4-CL has been formally identified by the United States Environmental Protection Agency as one of the most hazardous chemical pollutants [5]. Accordingly, the urgent development of innovative and highly effective strategies for the removal or detoxification of 4-CL from contaminated media is of paramount importance for protecting ecosystems and public health.

A broad spectrum of methods has been explored for the elimination of phenolic contaminants from environmental systems, with notable techniques including membrane-based separation, adsorption methodologies, and various advanced oxidation strategies [8–10]. However, conventional treatment methods—such as adsorption and membrane separation—are constrained by limited selectivity, membrane fouling, high operational costs, and the generation of secondary wastes [11, 12, 13]. These drawbacks motivate the adoption of photocatalytic oxidation, a cleaner and more sustainable alternative capable of deep-to-complete mineralization of chlorinated phenols under mild conditions [5, 14].

Advanced oxidation processes (AOPs)—such as the conventional Fenton reaction, photocatalysis, and the photo-Fenton method—have recently received widespread interest because of their exceptional effectiveness in breaking down persistent organic contaminants [14-19]. These oxidative techniques are regarded as both environmentally benign and technologically adaptable, particularly because they can harness solar energy, making them attractive options for large-scale and sustainable remediation efforts [5]. Consequently, significant research efforts have been invested in the synthesis and evaluation of diverse microstructured and nanostructured materials, aiming to exploit their multifunctionality in facilitating the degradation of organic contaminants alongside the reduction of hexavalent chromium [16, 20-23]. The effectiveness of a photocatalyst is governed by a range of parameters, including its structural and thermal stability, ability to be reused, ecological safety, suitable bandgap energy, electron–hole recombination behavior, adsorption efficiency, and economic viability [24, 25]. In alignment with goals for green chemistry and sustainable development, recent scientific discourse has emphasized the strategic use of naturally abundant precursors to engineer multifunctional materials. These bio-derived or mineral-based composites aim to offer synergistic photocatalytic and adsorptive efficiencies while remaining cost-effective and environmentally safe [26, 27]. This design also helps to minimize the common drawbacks of conventional photocatalysts, including rapid charge recombination, poor visible-light absorption, surface deactivation, photocorrosion, and low mineralization efficiency [11, 28, 29].

Zinc oxide (ZnO), in both nano- and microscale forms, is widely recognized for its effectiveness in oxidative degradation due to its high chemical stability, broad surface area,

non-toxic nature, and strong oxidative potential [26-30]. It also benefits from resistance to photocorrosion and a favorable exciton binding energy, making it highly suitable for photocatalysis [31-35]. To enhance its photocatalytic performance, strategies such as metal ion doping, composite integration, and nanoparticle immobilization have been widely explored, aiming to reduce charge recombination and improve light absorption and pollutant interaction [26, 36]. Nanostructured zinc-based photocatalysts demonstrate exceptional photocatalytic activity, long-term stability, and environmental safety, making them promising candidates for green and sustainable remediation technologies [37-39].

Within the field of photocatalytic science, bentonite has gained increasing recognition as an effective support material for heterogeneous catalysts [40, 41]. Bentonite (BEN), a naturally abundant phyllosilicate clay, is widely employed in environmental remediation due to its unique physicochemical characteristics [41, 42]. It offers a high cation exchange capacity, expansive surface area, abundant active sites, and an inherently non-toxic nature, making it particularly well-suited for dual functions—as a direct adsorbent and as a host matrix for metal and metal oxide catalysts [43, 44]. These attributes significantly improve both the functional and structural efficiency of photocatalytic systems when bentonite is incorporated as a supporting phase [42, 45]. The compositional profile of bentonite varies based on its smectite content, the type of associated mineral impurities, and their relative concentrations [46]. Of special interest are organic-rich bentonite variants, commonly referred to as oil shales, which remain relatively underutilized despite their wide availability [47]. These materials exhibit a unique hybrid structure that combines inorganic clay layers with intercalated organic substances such as kerogen and bitumen [47-49]. Chemical modification of these clay-organic composites, particularly through acid activation or sulfonation, can significantly enhance their surface polarity and introduce oxygenated functional groups [47-49]. This transformation increases their potential as acidic adsorbents and efficient catalyst supports [50-53].

This study introduces an innovative approach to the development of a cost-effective, eco-friendly, and high-performance photocatalyst for the efficient degradation of 4-chlorophenol (4-CL)—a persistent and toxic contaminant—commonly found in industrial wastewater. The research focuses on engineering a novel composite material by integrating

zinc oxide (ZnO), a widely studied photocatalyst, with sulfonated carbonaceous bentonite (SB), a naturally abundant yet underutilized clay-based support. The core objective is to harness the complementary functionalities of both components: the inherent adsorption capacity and surface acidity of sulfonated bentonite, and the strong oxidative and photocatalytic capabilities of ZnO. This synergistic integration is designed to enhance the removal efficiency of 4-CL through a dual mechanism involving surface adsorption and visible-light-driven photocatalytic oxidation. The novelty of this work lies in the strategic exploitation of carbon-rich, organic-intercalated bentonite—commonly overlooked in photocatalyst design—as a multifunctional platform. Through targeted sulfonation, the carbonaceous content of the bentonite is chemically activated to introduce robust acidic groups, while its layered silicate structure offers a high surface area for uniform ZnO dispersion. This tailored composite (ZnO@SB) is expected to exhibit enhanced photocatalytic activity, reusability, and stability under environmentally relevant conditions. By leveraging naturally available, low-cost mineral resources, this study not only addresses the urgent demand for sustainable treatment technologies for hazardous organic pollutants but also contributes to advancing the circular utilization of clay-based materials in the design of next-generation hybrid catalysts for environmental remediation.

2. Experimental work

2.1. Materials and chemicals

The bentonite used in this investigation was collected as a natural geological sample from Local quarries in Egypt. A detailed chemical composition analysis of the raw material revealed the presence of the following major oxides as the main composition: silicon dioxide (SiO_2) at 54.1%, aluminum oxide (Al_2O_3) at 24.73%, ferric oxide (Fe_2O_3) at 6.02%, magnesium oxide (MgO) at 1.09%, sodium oxide (Na_2O) at 0.09% , potassium oxide (K_2O) at 1.12 %, SO_3 at 1.78 %, and exhibited a loss on ignition (L.O.I) of 10.57 %. The synthesis of the ZnO@SB hybrid photocatalyst was performed using high-grade chemicals to ensure reproducibility and purity. Concentrated sulfuric acid (99%), absolute ethanol, and zinc nitrate hexahydrate ($Zn(NO_3)_2{\cdot}6H_2O$; 98%) were utilized, all acquired from Sigma-Aldrich (Egypt). For the evaluation of adsorption behavior and photocatalytic activity, 4-chlorophenol—chosen as a

model organic contaminant—was also obtained from Sigma-Aldrich, with a reported purity of 98%.

2.2. Synthesis of the photocatalyst

2.2.1. Acid activation of bentonite

The raw bentonite was ground using a ball mill to reduce the particle size to below 100 µm, ensuring uniform texture and consistency prior to the modification and synthesis steps. 80 grams of the resulting powder were then slowly added to 250 mL of sulfuric acid (70%), with the mixture maintained at a steady temperature of 100 °C. This acid-clay suspension was stirred continuously at 700 rpm for 12 hours, allowing the acid to thoroughly interact with the bentonite's layered structure. Once the reaction was complete, the mixture was left to cool naturally to room temperature. The solid product—now sulfonated bentonite (SB)—was collected through vacuum filtration using Whatman filter paper. To remove any leftover acid and soluble impurities, the filtered solid was rinsed five times with distilled water. Finally, the cleaned material was placed in oven at 75 °C for about 4 hours to ensure it was fully dehydrated and ready for use (Fig. 1).

2.2.3. Preparation of ZnO@SB hybrid material

The ZnO@SB hybrid material was synthesized by dispersing 10 grams of sulfonated bentonite (SB) into 100 mL of an aqueous solution containing 10 grams of zinc nitrate. To ensure effective interaction between the zinc ions and the functional groups on the bentonite surface, the mixture was stirred continuously at 650 rpm for 10 hours. This was followed by ultrasonic treatment for 2 hours using a 240-watt ultrasonic generator, which helped enhance dispersion of the metal precursor and encouraged its incorporation into the clay structure. Subsequently, 100 mL of a 0.1 mM sodium hydroxide solution was slowly added to the suspension under constant stirring. The reaction was allowed to proceed for another 6 hours to promote the controlled precipitation of zinc species. To further support the formation and uniform distribution of ZnO within the clay matrix, the mixture was heated at 100 °C for 24 hours, with ultrasonic activation applied every 6 hours and continuous stirring maintained at 700 rpm. After the synthesis was complete, the solid ZnO@SB composite was separated by filtration using Whatman filter paper. It was then thoroughly washed with distilled water through five rinsing cycles (10 minutes each) to remove any unreacted materials and soluble

byproducts. Finally, the purified material was dried in an oven at 80 °C for 12 hours, yielding the ZnO-functionalized bentonite hybrid (Fig. 1).

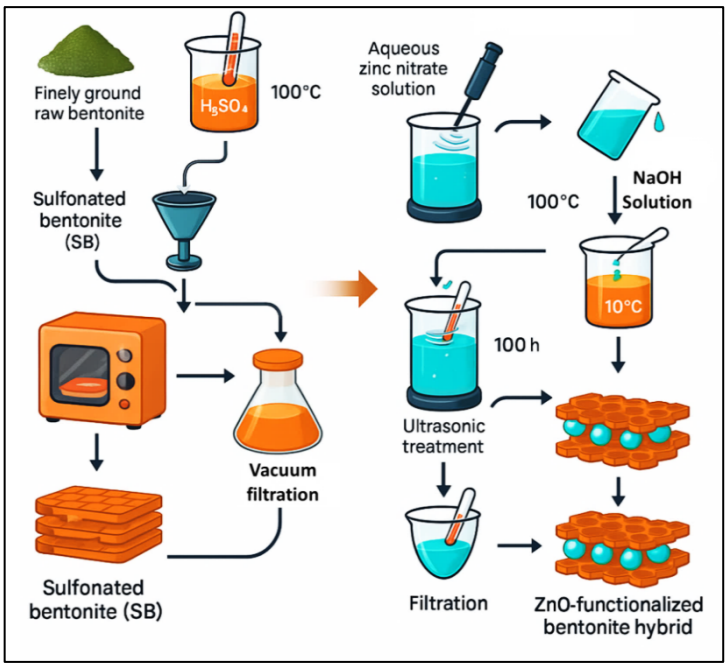

Fig.1. Schematic diagram for the synthesis of ZnO@SB composite. *Created by the authors in Adobe Illustrator v29.8.1 (Adobe Inc., https://www.adobe.com/products/illustrator.html).*

2.4. Characterization techniques

To assess the structural and physicochemical properties of the synthesized materials, a range of analytical techniques was employed. The crystalline phases and structural changes occurring during synthesis were examined using X-ray diffraction (XRD), performed on a PANalytical Empyrean diffractometer operating within a 2θ range of 5° to 80°. Functional groups and chemical modifications were identified through Fourier-transform infrared spectroscopy (FT-IR) using a Shimadzu FTIR-8400S, with spectra collected across the range of 400–4000 cm^{-1}. The surface morphology and particle structure were visualized using scanning electron microscopy (SEM, Zeiss Ultra 55), following gold sputter-coating of the samples to enhance conductivity. Additionally, nitrogen adsorption–desorption isotherms were measured with a Beckman Coulter SA3100 surface area analyzer, after degassing the samples. These measurements provided insights into surface area and porosity—key parameters for evaluating the material's potential in adsorption and photocatalytic applications.

2.5. Advanced oxidation of 4-CL

The photocatalytic potential of the ZnO-functionalized sulfonated bentonite (ZnO@SB) composite was thoroughly investigated through the degradation of 4-chlorophenol (4-CL)

under visible light exposure. Experiments were conducted in a vertically oriented Pyrex glass reactor, measuring 7 cm in diameter and 15 cm in height, which was engineered to maximize both light transmission and photocatalyst suspension uniformity. Illumination was provided by a 400-watt commercial metal halide lamp, emitting predominantly visible light with a characteristic wavelength around 490 nm. The lamp was positioned 3.5 cm from the external wall of the reactor, providing a consistent light intensity across the sample volume. Light irradiance at the reactor surface was measured at an average of 18.7 milliwatts per square centimeter, effectively mimicking solar irradiation conditions suitable for environmental applications.

Before initiating visible-light irradiation, all photocatalytic experiments were preceded by an adsorption–desorption equilibration step to ensure that any subsequent decrease in 4-CL concentration was exclusively attributed to photocatalytic activity. For this purpose, the reaction suspension containing the photocatalyst and pollutant solution was stirred continuously in the dark for 30 minutes to attain adsorption equilibrium between the solid surface and the aqueous phase. After equilibrium was established, illumination was started under the same stirring conditions to commence the photocatalytic degradation experiment.

The photocatalytic experiments were conducted under ambient temperature (approximately 20 °C). During testing, the initial concentration of 4-CL varied from 5 mg/L to 20 mg/L, while the ZnO@SB photocatalyst loading was adjusted incrementally from 0.2 to 0.5 g/L. The reaction durations ranged from 5 minutes up to 240 minutes, enabling detailed observation of kinetic trends, pollutant breakdown efficiency, and the influence of varying pollutant concentrations and photocatalyst dosages.

After each trial, the amount of un-degraded 4-CL remaining in the solution was quantified to assess both the initial adsorption equilibrium and the extent of photocatalytic oxidation. All experimental runs were repeated three times to verify reproducibility, with observed standard deviations consistently under 3.5%, confirming the reliability of the methodology. To further elucidate the degradation process and identify transformation products, high-performance liquid chromatography system (HPLC 3000) equipped with a Thermo analytical column analysis was performed. In addition, total organic carbon (TOC) analysis was conducted using a Shimadzu TOC-VCPH analyzer to measure the degree of

mineralization. This step was essential for determining the photocatalyst's effectiveness in breaking down 4-CL into non-toxic, low-molecular-weight byproducts, thus providing a complete picture of the material's photocatalytic efficiency.

3. Results and discussion

3.1. Characterization of the photocatalyst:

3.1.1. X-ray diffraction (XRD) analysis

The structural modifications imparted throughout the multistep synthesis were meticulously characterized using XRD analysis, providing vital insights into the crystallographic transformations occurring at each functionalization stage (Fig. 2). The initial diffraction profile of the raw carbonaceous bentonite-based material (CB) exhibited pronounced reflections consistent with a montmorillonite-dominant mineralogy. Notably, peaks at 2θ = 6.05° (002), 19.77° (020), and 25.1° (105) aligned well with standard reference patterns from JCPDS cards 00-003-0010 and 00-058-2010 (Fig. 2A), affirming the layered silicate structure characteristic of unmodified bentonite [50]. However, subtle deviations in peak positions and intensities, compared to typical montmorillonite, were evident—an indication of structural perturbation likely caused by the intercalation of native organic moieties such as kerogen or maceral derivatives. These organic components, commonly found in carbon-rich bentonites, are known to insert into the interlayer space, resulting in a basal spacing expansion. This interpretation is strongly supported by the measured increase in interlayer distance to ~14.59 Å, significantly exceeding that of standard montmorillonite (Fig. 2A). Such interlayer swelling confirms the successful organo-modification of the clay—transforming it into an organoclay matrix with enhanced functionality and affinity for further chemical modification.

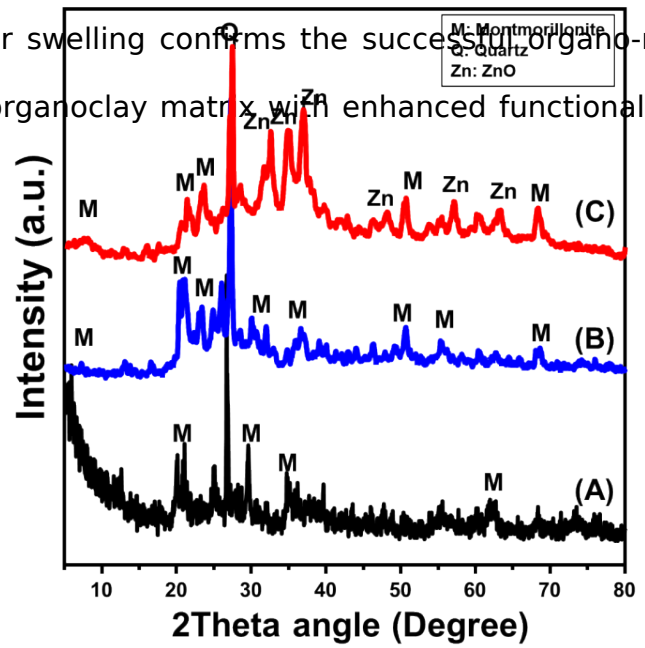

Fig.2. XRD patterns of raw carbonaceous bentonite (A) [50], sulfonated sample (B) and synthetic ZnO/SB photocatalyst (C)

Subsequent sulfonation of the composite yielded a material (SB) with a markedly altered diffraction pattern, reflecting substantial changes in the crystalline order of the support (Fig. 2B). A noticeable reduction in the intensity and clarity of montmorillonite peaks—alongside peak broadening and in some cases, complete disappearance—suggests structural degradation induced by acid leaching (Fig. 2B). This phenomenon is attributed to the partial dissolution of key lattice cations, such as Si^{4+} and Al^{3+}, which are fundamental to the tetrahedral and octahedral layers of the montmorillonite framework [47]. As these cations are selectively extracted under acidic conditions, the clay undergoes partial exfoliation and loses long-range periodicity, leading to increased disorder within the layered architecture. Furthermore, the strong oxidizing environment associated with sulfonation promotes the cleavage of thermally and chemically labile linkages—particularly ether bonds (C–O–C)—within the intercalated organic matrix [54, 55]. This oxidative fragmentation contributes to partial amorphization of the hybrid structure while simultaneously enriching the surface with acidic functional groups, predominantly sulfonic acid ($–SO_3H$). These newly introduced moieties significantly enhance the composite's surface reactivity and potential for catalysis, providing both Brønsted acid sites and coordination centers for metal anchoring.

The final ZnO-functionalized composite (ZnO@SB) displayed a complex XRD signature, indicative of successful integration of crystalline ZnO nanoparticles onto the modified bentonite substrate (Fig. 2C). While a residual basal reflection of bentonite was still detectable at $2\theta \approx 7.12°$, its diminished intensity and minor shift implied a partial preservation of the original clay structure, now altered by successive chemical treatments (Fig. 2C). Superimposed on this pattern were distinct and sharp peaks at 2θ values of 31.75°, 34.85°, 36.61°, and 47.6°, corresponding to the (100), (002), (101), and (102) planes of hexagonal wurtzite ZnO (Fig. 2C) (JCPDS Nos. 65-3411, 36-1451). These reflections unambiguously confirm the successful crystallization of ZnO, with an estimated crystallite size of ~34 nm—

well within the nanometric regime and favorable for enhanced photocatalytic efficiency. Interestingly, a systematic shift of certain ZnO peaks toward lower diffraction angles was observed, which may signal lattice distortion caused by strong interactions between Zn^{2+} ions and the sulfonic acid groups anchored on the bentonite surface. This suggests possible surface complexation or partial intercalation of zinc species within the clay matrix, inducing strain within the ZnO lattice. Such structural coupling implies a tightly bound interface between the metal oxide and its support, which is crucial for charge transfer, pollutant adsorption, and photocatalytic turnover.

From an application standpoint, these structural and chemical features collectively point to the formation of a multifunctional photocatalyst with synergistic properties. Acidic sites introduced by H_2SO_4 activation increase surface polarity and adsorption affinity, promoting pollutant accumulation and diffusion to active centers [56, 57]. Nanocrystalline ZnO domains enhance light absorption and charge separation by exposing polar facets [58, 59]. Meanwhile, the hierarchically porous framework improves mass transport, active-site accessibility, and photon utilization, accelerating degradation kinetics [60, 61]. This engineered heterostructure thus provides an efficient platform for the removal of persistent pollutants such as 4-chlorophenol, where adsorption–photocatalysis coupling is crucial for high-performance remediation.

3.1.2. Scanning electron microscopy (SEM) analysis

The morphological evolution of carbonaceous bentonite throughout its stepwise chemical modification was carefully tracked using scanning electron microscopy (SEM) (Fig. 3). In its raw form, the carbonaceous bentonite (CB) exhibited a typical clay-like morphology, with dense aggregates of irregularly stacked platelets forming bulky, compact masses (Fig. 3A). These layered structures are characteristic of smectite-type clays, which naturally possess lamellar arrangements due to their silicate framework. Closer inspection also revealed the presence of fine, spherical particulates scattered across the surface (Fig. 3A), which are likely associated with organic components—possibly kerogen or other carbonaceous residues—embedded within or adhered to the clay layers. These organic inclusions not only contribute to the physical heterogeneity of the material but may also play a role in its chemical reactivity, providing potential sites for further functionalization.

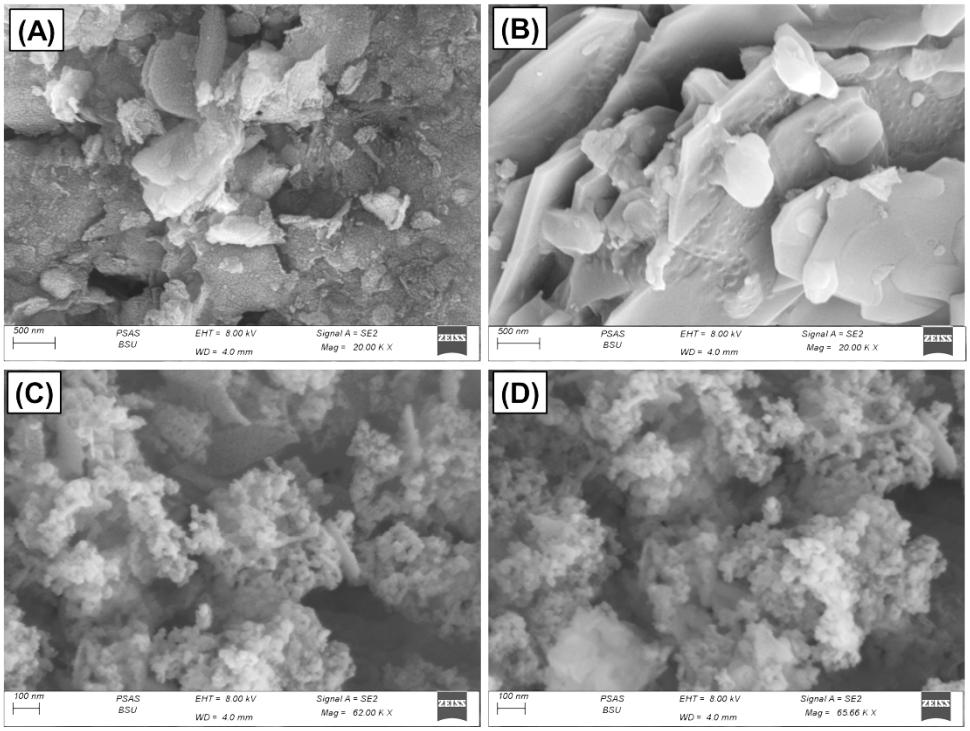

Fig.3. SEM images of carbonaceous bentonite (A), sulfonated sample (B), and synthetic ZnO/SB hybrid (C and D)

Following sulfonation with concentrated H_2SO_4, the bentonite underwent marked surface transformation. The sulfonated material (SB) displayed smoother surfaces compared to the unmodified CB (Fig. 3B), suggesting that the acid treatment effectively removed surface-bound impurities and partially decomposed organic matter. This "cleaning" action likely results from both the oxidative strength and acidity of H_2SO_4, which can break down labile bonds within organic fragments while simultaneously altering the surface topography. Interestingly, despite the smoother appearance, the sulfonated samples also showed an increase in porosity and surface roughness at a finer scale. SEM images (Fig. 3B) revealed uneven edges and pore-like features across the particle surfaces—evidence of mineral leaching and microstructural etching brought about by acid attack. From a photocatalytic standpoint, this is highly advantageous: greater porosity improves accessibility to active sites, while surface acidity enhances interactions with pollutant molecules during degradation processes.

After ZnO deposition, the final ZnO@SB composite presented a clearly distinct morphology. SEM images (Fig. 3C and D) showed that ZnO nanoparticles formed a uniform, interlinked layer over the sulfonated clay surface. The nanoparticles appeared as aggregated nano-grains with slightly curved, worm-like geometries, resulting in a porous and texturally rich structure. This hierarchical assembly supports both high surface area and efficient mass

transport—two key requirements for photocatalytic systems operating under flow or batch conditions. The homogeneous distribution of ZnO suggests strong binding between the nanoparticles and the sulfonated bentonite surface, likely facilitated by coordination with sulfonic acid groups. These interactions may contribute to improved electron transfer and photocatalytic activation. Mechanically, the ZnO layer reinforces the structural stability of the composite, while functionally, it introduces redox-active centers capable of driving photocatalytic and oxidative degradation reactions.

3.1.3. Fourier-transform infrared (FTIR) spectroscopy analysis

Fourier-transform infrared (FT-IR) spectroscopy was employed to monitor the progressive chemical and structural transformations of natural bentonite (NB), organically enriched carbonaceous bentonite (CB), and the sulfonated bentonite-based photocatalyst (SB). Figure 4 presents the comparative spectra, which elucidate the changes at each stage of synthesis, offering insight into the development of functional groups critical to adsorption and photocatalytic activity. The FT-IR spectrum of the unmodified natural bentonite (NB) displayed well-resolved vibrational bands characteristic of montmorillonite-type clay minerals (Fig. S1). A broad absorption envelope in the 3100–3700 cm^{-1} range was attributed to the stretching vibrations of structural –OH groups, including those from interlayer water and lattice hydroxyls (Fig. S1). The sharp peak at 1640.6 cm^{-1} corresponds to the bending vibration of adsorbed H_2O, while prominent signals at 1000.3 cm^{-1} and 918.2 cm^{-1} were assigned to Si–O stretching and Al–O vibrational modes, respectively. Additional features in the 400–1000 cm^{-1} region were consistent with Si–O–Mg, Fe–OH, and Si–O–Al bending vibrations, affirming the integrity of the layered silicate framework [46, 47] (Fig. S1).

For carbonaceous bentonite (CB), the core mineral structure was largely retained, as evidenced by the persistence of montmorillonite bands. However, new absorption features emerged, revealing the successful intercalation of organic matter within the clay matrix (Fig. 4A). Notably, a band at 2924.8 cm^{-1} was observed, corresponding to C–H stretching vibrations of aliphatic chains, while signals at 1620 cm^{-1} and 1428 cm^{-1} were assigned to C=O bending and C–OH deformation, respectively (Fig. 4A) [47, 55]. These spectral changes are indicative of kerogen-like or maceral organic compounds being incorporated into the interlayer space or adsorbed onto the surface. The formation of this hybrid organic–inorganic structure is

significant, as it enhances surface heterogeneity and offers reactive sites for subsequent chemical functionalization.

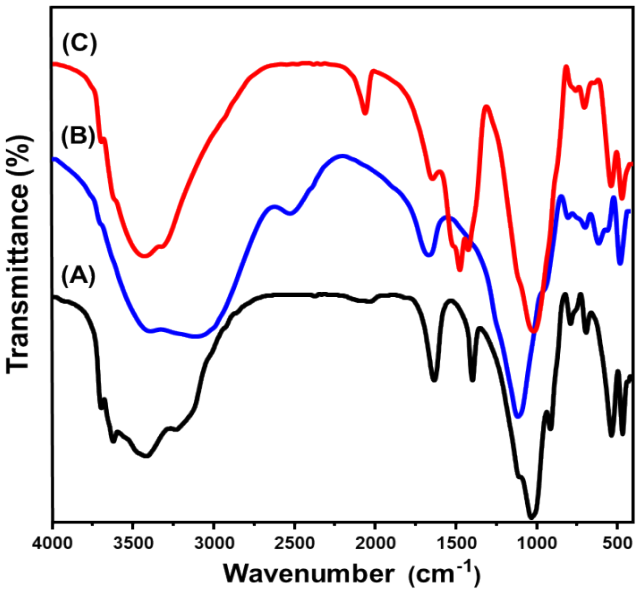

Fig. 4. FT-IR spectra of carbonaceous bentonite (A) [50], sulfonated sample (B), and synthetic ZnO/SB hybrid (C)

Following sulfonation, the FT-IR spectrum of the SB sample revealed significant alterations in both its mineralogical and organic functional group profiles (Fig. 4B). The –OH stretching band became noticeably broader and diminished in intensity, a change that is indicative of the formation of carboxylic acid (–COOH) functionalities (Fig. 4B). This transformation is likely a result of the oxidative breakdown of native organic constituents under the highly acidic treatment conditions [50, 62, 63]. Additionally, the weakening of hydroxyl-related bands also suggests partial dehydroxylation of the clay structure and the removal of physically adsorbed water molecules, both of which are consistent with acid-induced structural reorganization and leaching. A new, broad band around ~2516 cm^{-1} appears, commonly attributed to O–H stretching in strongly hydrogen-bonded carboxylic acids (–COOH) (Fig. 4B). Its presence suggests the oxidative introduction of proton-donating acidic groups, which complements the sulfonic functionality and enhances surface reactivity. The complete reduction of the detected band around 1428 cm^{-1} (CH or C–OH bending) in the CB sample, demonstrate the extensive oxidation and destruction effect of the sulfuric acid on the existed organic matters (Fig. 4B). This might be associated with chemical evolution toward more acidic, catalytically relevant functional groups.

The disappearance of this band, coupled with the appearance of strong S=O stretches and the broad O–H band near 2516 cm^{-1} in the SB spectrum, collectively signals loss of

weakly bound or passive organic matter, and creation of chemically active, polar functional groups, such as sulfonic and carboxylic acids, which are better suited for adsorption and photocatalytic performance (Fig. 4B) [64, 65]. Changes in the Si–O stretching region (~1000–1100 cm^{-1}) imply partial disruption of the silicate layers, likely caused by the leaching of framework cations (e.g., Si^{4+}, Al^{3+}, Mg^{2+}) during acid treatment as well as possible overlap with the incorporated (O=S=O) groups during the suflonation process. A new absorption band observed at ~598 cm^{-1} in the SB spectrum can be assigned to S–O or S-C bending vibrations, further confirming the presence of sulfonic acid groups (–SO_3H) introduced during acid treatment [66, 67] (Fig. 4B). These groups are particularly valuable as they enhance acidity and surface polarity, facilitating stronger interactions with target pollutants in photocatalytic applications.

Upon incorporation of ZnO, the FT-IR spectrum of ZnO@SB revealed both the retention and transformation of these key features (Fig. 4C). The sulfonic bands remained visible but exhibited slight shifts to lower wavenumbers and increased broadening, likely due to electrostatic interactions or coordination between Zn^{2+} ions and sulfonate groups [68]. This observation indicates the chemical stability of sulfonic functionalities, even after metal oxide loading, and their potential role in anchoring ZnO particles within the clay matrix. The most prominent change in the ZnO@SB spectrum was the appearance of a strong band near ~490–510 cm^{-1}, which is characteristic of Zn–O stretching vibrations from the crystal structure of ZnO nanoparticles (Fig. 4C) [69, 70]. This band was absent in the SB spectrum, serving as direct evidence of ZnO formation and confirming successful composite synthesis. Additionally, significant changes were observed in the region between ~1472 and 1420 cm^{-1}, where new bands emerged that are consistent with asymmetric and symmetric stretching of coordinated carboxylate (–COO^-) or sulfonate groups (Fig. 4C). These features, coupled with the diminution or disappearance of the broad ~2500 cm^{-1} band, suggest that Zn^{2+} ions engaged in coordination interactions with pre-existing carboxylic and sulfonic acid sites, forming stable metal–ligand complexes during synthesis. Such interactions contribute to the chemical integrity of the composite and may facilitate interfacial electron transfer during photocatalysis.

Taken together, the FT-IR comparison between SB and ZnO@SB highlights the retention of surface acidity, the successful formation of ZnO nanophases, and the development of strong chemical interactions at the oxide–support interface. These structural features directly contribute to the catalyst's dual-function performance. The acidic surface groups support adsorption and pre-concentration of chlorophenol molecules, while the ZnO domains provide active redox sites for photocatalytic degradation. The interplay between these functionalities is essential for enhancing both the efficiency and selectivity of 4-chlorophenol removal under visible light conditions.

3.1.4. Energy dispersive X-ray (EDX) analysis

Energy Dispersive X-ray (EDX) spectroscopy was employed to confirm the elemental composition and validate the successful chemical modification of the synthesized materials, in agreement with prior structural and spectroscopic analyses (Fig. S2). The EDX profile of the sulfonated bentonite (SB) displayed prominent signals corresponding to oxygen (O), silicon (Si), and aluminum (Al)—the principal constituents of the aluminosilicate lattice inherent to bentonite clays (Fig. S2). In addition, the presence of carbon (C) was attributed to residual organic phases within the carbonaceous matrix, while a well-defined sulfur (S) peak provided direct evidence for the successful incorporation of sulfonic acid groups (–SO_3H) (Fig. S2). The detection of sulfur is particularly significant, as it confirms the chemical grafting of functional acid moieties onto the clay surface—an essential modification aimed at improving surface acidity, polarity, and adsorption potential. These findings indicate that the sulfonation process effectively altered the surface chemistry of the raw clay, enhancing its photocatalytic and adsorptive properties without compromising the integrity of the core mineral framework. The presence of these acidic sites plays a pivotal role in pollutant uptake and in facilitating charge interaction with target molecules, thereby improving overall reactivity.

For the ZnO-functionalized composite (ZnO@SB), the EDX spectrum showed the continued presence of the original framework elements (Si, Al, O, and C), indicating that the structural backbone of the sulfonated bentonite was retained post-modification (Fig. S2). Most notably, a distinct zinc (Zn) signal was observed, confirming the successful deposition and incorporation of zinc oxide (ZnO) into the sulfonated clay matrix (Fig. S2). This integration is critical, as ZnO introduces catalytically active redox centers that serve as electron donors and

acceptors during photocatalytic reactions. The uniform distribution of Zn also suggests effective dispersion of nanoparticles across the support surface, which is essential for maximizing photocatalytic efficiency. Therefore, the EDX analysis confirms both the chemical functionalization of bentonite with sulfonic groups and the subsequent loading of ZnO nanoparticles, both of which are central to the material's dual functionality in adsorptive enrichment and photocatalytic degradation of organic contaminants.

3.1.5. Textural studies

The textural characteristics of the ZnO-functionalized sulfonated bentonite composite (ZnO@SB) were comprehensively evaluated using nitrogen adsorption–desorption analysis, as illustrated in Figure 5A, alongside pore size distribution data presented in Figure 5B. The nitrogen adsorption–desorption isotherm of ZnO@SB exhibits a typical Type IV profile with a distinct H3 hysteresis loop, in line with the International Union of Pure and Applied Chemistry (IUPAC) guidelines (Fig. 5A). This pattern is emblematic of mesoporous structures, particularly those composed of aggregates of plate-like particles forming slit-shaped pores. The presence of this hysteresis suggests multilayer adsorption followed by capillary condensation, indicative of well-organized mesoporosity [71, 72]. The progressive increase in nitrogen uptake across the low to intermediate relative pressure range (P/P_0 = 0.0–0.8) reflects gradual pore filling, while the pronounced uptake at higher relative pressures ($P/P_0 > 0.9$) implies the presence of interparticle voids or larger mesopores that contribute to hierarchical porosity. Such hierarchical features are commonly associated with improved mass transfer properties, which are vital in catalysis where reactants and products must navigate through the porous network [73].

The pore size distribution curve reveals a dominant pore diameter within the range of 4 to 10 nm, with a significant peak centered at approximately 7.8 nm (Fig. 5B). This confirms the mesoporous framework of the composite. The relatively narrow distribution and centered peak suggest that the ZnO nanoparticles were effectively dispersed within the sulfonated bentonite matrix, ensuring structural integrity without blocking or collapsing the native pore network. Such uniformity is essential for sustaining high surface area and maintaining reactive site accessibility. The measured Brunauer–Emmett–Teller (BET) surface area of ZnO@SB is 78.6 m^2/g, and the total pore volume stands at 0.1291 cm^3/g. The BET surface

area measured for ZnO@SB (78.6 m^2/g) is above typical values for unsupported ZnO nanoparticles (commonly ~12–35 m^2/g) and in the same band as H_2SO_4-activated/bentonite-based acids (~50–70 m^2/g). Moreover, recent ZnO–bentonite hybrids show type-IV (H4) N_2-sorption isotherms and larger specific areas than bare ZnO, consistent with enhanced mesoporosity and surface accessibility [74-77]. These values reflect a substantial degree of internal porosity and surface exposure, both of which are advantageous for photocatalytic and adsorptive applications. A high surface area promotes greater availability of active sites, while a well-developed pore volume supports efficient transport of reactant molecules and rapid diffusion kinetics. Notably, the coexistence of mesopores and larger voids (inter-aggregate spaces) introduces a multi-scale porosity that offers dual functional benefits: enhanced adsorption capacity due to increased surface sites, and improved photonic and molecular transport within the material matrix. This structural arrangement is particularly beneficial in photocatalytic systems, where both light harvesting and molecule diffusion are rate-determining steps.

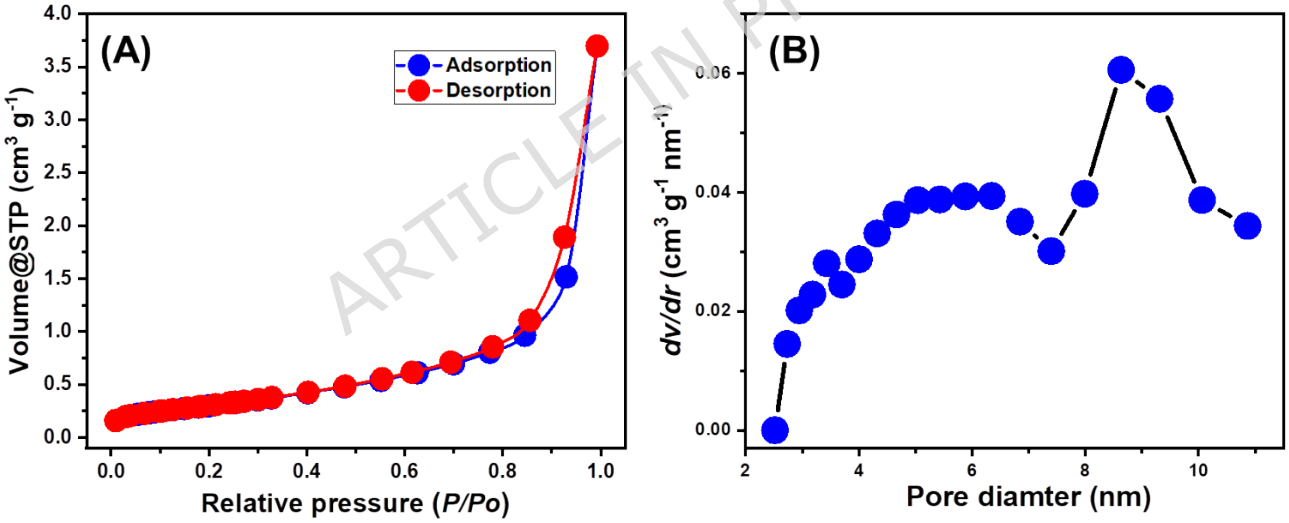

Fig.5. Nitrogen adsorption/desorption isotherm curve (A) and pore size distribution curve (B) of ZnO@SB

3.1.6. Optical properties

The optical properties of the ZnO@SB composite were evaluated using UV–Vis spectroscopy. The spectrum exhibits a strong absorption band in the UV region, followed by a gradual decrease in intensity toward longer wavelengths (Fig. S3). This behavior is typical of ZnO-based materials and reflects the fundamental band-to-band transitions of ZnO nanocrystals, together with a weak visible-light tail associated with defect-related states and interfacial electronic interactions with the sulfonated carbonaceous bentonite matrix [78, 79].

The modest but non-negligible visible-range absorbance suggests the presence of localized states or electronic coupling at the ZnO–support interface, which subtly modifies the optical response of the hybrid material, as reported for other ZnO/clay and ZnO/carbon composites. The optical band gap of ZnO@SB, estimated from the Tauc plot assuming a direct allowed transition, was approximately 2.75 eV, lower than that of bulk ZnO (≈3.2–3.3 eV) [80-82].

This reduction indicates a red shift of the absorption edge toward the visible domain and is consistent with literature on defect-rich and carbon-modified ZnO/clay systems, where band-gap narrowing is attributed to oxygen-vacancy states, interfacial defect levels, and charge-transfer interactions with carbonaceous and mineral supports. In the present system, the sulfonated carbonaceous bentonite provides both acidic and π-conjugated functional groups that can interact electronically with ZnO, promoting the formation of interfacial states and facilitating charge delocalization at the ZnO/SB interface [83-85].

The narrowed band gap and red-shifted absorption edge enhance the ability of ZnO@SB to utilize the visible fraction of the metal-halide light employed in this study, thereby increasing the generation of electron–hole pairs under irradiation. This enhanced optical response is consistent with radical-scavenging experiments, which identified hydroxyl and superoxide radicals as the predominant reactive oxygen species responsible for 4-CL degradation. The improved radical formation can be ascribed to more efficient photon harvesting, facilitated charge separation, and the participation of interfacial electronic states created through coupling of ZnO with the sulfonated bentonite substrate. Overall, the UV–Vis and Tauc analyses indicate that ZnO@SB possesses a modified electronic structure and enhanced visible-light responsiveness compared with pristine ZnO. When combined with the mesoporous nature and high adsorption capacity of the bentonite-based support, these optical and electronic features provide a robust basis for the superior photocatalytic performance of ZnO@SB relative to unmodified ZnO and several conventional ZnO-based photocatalysts reported in the literature.

3.2. Photocatalytic degradation results

3.2.1. Effect of oxidation parameters

3.2.1.1. Effect of pH

The pH of the aqueous medium significantly influences both the surface charge distribution of the ZnO@SB composite and the ionization behavior of water-soluble organic compounds such as 4-chlorophenol (4-CL) [86]. To investigate this relationship, the adsorption efficiency of ZnO@SB was evaluated across a pH range of 3 to 10, under controlled conditions: contact time of 60 minutes, temperature of 20 ^{o}C, solution volume of 50 mL, 4-CL concentration of 5 mg/L, and an adsorbent dosage of 0.2 g/L. The results demonstrated a pronounced pH-dependent trend. Oxidation efficiency increased with pH, reaching a maximum of 90.7% at pH 8 (Fig. 6), followed by a sharp decline under alkaline conditions (pH 10) (Fig. 6). This behavior is governed by both surface chemistry and the speciation of 4-CL in aqueous media. At low pH values, the surface of ZnO@SB tends to be positively charged, while the abundance of H^+ ions leads to competition with 4-CL molecules for adsorption sites, thereby reducing adsorption capacity [87].

As the pH increases toward neutrality, the electrostatic repulsion diminishes, and 4-CL—whose pKa ranges between 4.7 and 9.4—partially dissociates into its anionic form [72]. This transition promotes stronger interactions between the negatively charged 4-CL and the relatively neutral or slightly positive adsorbent surface, enhancing adsorption. The peak adsorption at pH 8 is attributed to an optimal balance between surface charge conditions and the molecular speciation of 4-CL. At alkaline pH values above 9, both 4-CL and the ZnO@SB surface acquire negative charges, leading to strong electrostatic repulsion. This reduces the availability of 4-CL molecules at the photocatalyst surface, resulting in significantly diminished adsorption performance [88].

In heterogeneous photocatalytic systems such as this, efficient oxidation relies heavily on the initial adsorption of the pollutant onto the photocatalyst surface. This proximity facilitates effective electron transfer and interaction with oxidizing radicals, such as hydroxyl radicals (•OH) and superoxide anions ($O_2^{\bullet -}$), which are generated during photocatalytic activation. At optimal pH (8), where adsorption is maximized, a higher concentration of 4-CL is localized on the photocatalyst surface, enabling rapid and effective oxidation. In contrast, under acidic or strongly alkaline conditions where adsorption is limited, fewer pollutant molecules are available at the active sites, resulting in lower degradation rates. Moreover, poor adsorption at high pH also reduces the interaction between 4-CL and ROS, further

hindering oxidation kinetics. These observations reinforce the synergistic relationship between adsorption and oxidation processes in photocatalytic systems. Optimizing pH not only enhances the initial capture of pollutants but also directly improves the efficiency of their subsequent degradation. Therefore, controlling pH is critical for maximizing the overall performance of ZnO@SB in advanced oxidation processes targeting 4-CL.

Fig.6. Experimental influence of the solution pH on the oxidation of 4-CL using ZnO@SB

3.2.1.2. Effect of 4-CL contents at different periods

The photocatalytic performance of ZnO@SB composites was systematically investigated as a function of reaction time (ranging from 5 to 240 minutes) and varying initial concentrations of 4-chlorophenol (4-CL) from 5 to 20 mg/L. Throughout the experimental procedures, key parameters were meticulously controlled to ensure consistency: photocatalyst dosage was maintained at 0.2 g/L, the reaction volume at 50 mL, pH at 8, and temperature at a constant 20 °C. The ZnO@SB material demonstrated pronounced photocatalytic activity, facilitating rapid degradation of 4-CL in relatively short timeframes (Fig. 7A). Notably, complete removal (100%) of 4-CL was achieved at an initial concentration of 5 mg/L within 80 minutes. For higher concentrations—namely 10 mg/L and 15 mg/L—the same removal efficiency was attained at extended durations of 120 and 240 minutes, respectively (Fig. 7A), highlighting the time-dependent nature of the degradation process in relation to pollutant load.

However, as the initial concentration of 4-CL increased, a noticeable decline in photocatalytic efficiency was observed (97.8%; 20 mg/L after 240 minutes). This phenomenon

643 can be attributed to the development of densely packed adsorption layers of 4-CL molecules
644 on the ZnO@SB surface. Such layers hinder the accessibility of active sites and suppress the
645 effective interaction between the photocatalyst and incident light, as well as between reactive
646 species and the substrate molecules. The excessive accumulation of 4-CL reduces light
647 penetration, thereby impeding the generation of hydroxyl and other reactive radicals
648 essential for oxidative degradation [89]. Moreover, the gradual attenuation in degradation
649 efficiency over prolonged reaction times suggests the depletion of reactive oxidative species
650 as the reaction progresses. Once the radicals generated by the photocatalyst are consumed—
651 particularly in high pollutant concentrations—the rate of degradation plateaus, and the
652 system approaches an equilibrium state. This stagnation implies a dynamic balance where
653 radical generation no longer compensates for the demand, resulting in marginal further
654 degradation of 4-CL. This behavior is consistent with previous findings that reported a
655 decrease in oxidative decomposition efficiency due to radical exhaustion during prolonged
656 photocatalytic processes [90]. These results underscore the significance of optimizing
657 pollutant load and reaction duration to achieve maximum photocatalytic efficiency. The
658 findings also highlight potential challenges in scaling this process for treatment of wastewater
659 with high concentrations of recalcitrant organic pollutants, indicating the necessity for
660 enhanced photocatalyst design or multi-stage treatment strategies.
661

662 **3.2.1.3. Effect of ZnO@SB dosages at different periods**

663 The impact of varying ZnO@SB photocatalyst dosages on the photocatalytic
664 degradation of 4-chlorophenol (4-CL) was comprehensively investigated. Dosage levels were
665 adjusted from 0.2 g/L to 0.5 g/L to evaluate their effect on the decomposition efficiency of
666 different 4-CL concentrations (5–20 mg/L). The photocatalytic oxidation was conducted over a
667 time range of 5 to 240 minutes, with all other operational conditions held constant: reaction
668 volume (50 mL), temperature (20 °C), and pH (8). The results revealed a strong correlation
669 between increased photocatalyst dosage and enhanced degradation performance (Fig. 7B-E).
670 For instance, at a 4-CL concentration of 5 mg/L, complete degradation was achieved within 80
671 minutes using 0.2 g/L of ZnO@SB (Fig. 7B). When the dosage was increased to 0.4 g/L and 0.5
672 g/L, the time required for full oxidation was significantly reduced to 40 and 30 minutes,

673 respectively (Fig. 7B). Similar trends were observed at higher pollutant concentrations: for 10
674 mg/L of 4-CL, complete removal was reached in 120 minutes with 0.2 g/L, compared to only
675 80 and 60 minutes when using 0.4 g/L and 0.5 g/L, respectively (Fig. 7C).

676 At a concentration of 15 mg/L, a marked improvement in degradation efficiency was
677 also evident. Complete removal was achieved in just 100 minutes at 0.5 g/L, in contrast to the
678 240 minutes required with 0.2 g/L (Fig. 7D). For the highest tested concentration (20 mg/L),
679 full degradation was accomplished in 240 minutes using 0.4 g/L and was further reduced to
680 180 minutes with a 0.5 g/L photocatalyst dose (Fig. 7E). These findings clearly indicate that
681 increasing the ZnO@SB dosage significantly enhances photocatalytic activity. This
682 improvement is attributed to the greater availability of active photocatalytic sites and a
683 higher surface area for interaction, which collectively facilitate more efficient generation and
684 utilization of reactive species (ROS), such as hydroxyl radicals, during the oxidation process
685 [36, 91]. The enhanced photocatalyst loading intensifies the contact probability between the
686 4-CL molecules and the active surface of ZnO@SB, thereby accelerating the degradation
687 kinetics. Furthermore, the observed dosage-dependent performance suggests that the
688 photocatalyst quantity directly influences the extent and rate of oxidative transformations,
689 particularly in systems with elevated pollutant loads. However, it is essential to balance
690 photocatalyst dosage to avoid potential drawbacks such as light scattering or agglomeration
691 at excessive concentrations, which may reduce the effective surface area or hinder photon
692 absorption efficiency. In summary, optimizing the dosage of ZnO@SB is critical for maximizing
693 degradation performance, especially when targeting varying concentrations of persistent
694 organic contaminants. The data underscores the photocatalyst's potential for scalable
695 application in wastewater treatment scenarios where tailored dosages can ensure both high
696 efficiency and cost-effectiveness.

697 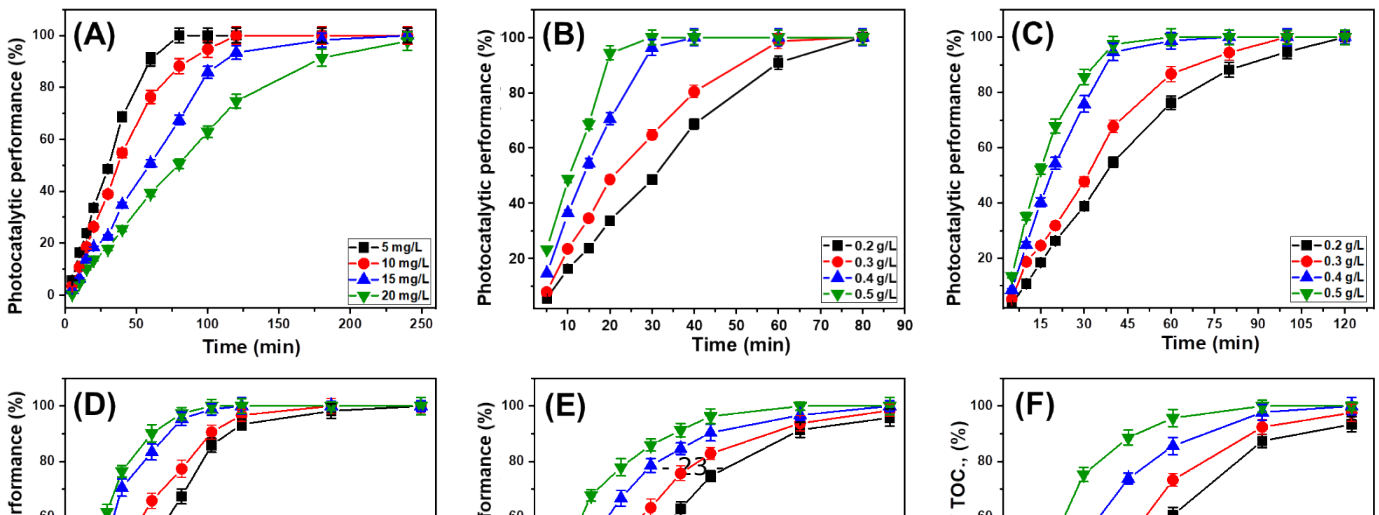

Fig.7. Experimental influence starting 4-CL content of 4-CL versus time (A) (Notice 5, 10, 15, and 20 mg/L pollutant concentration), incorporated dosage of the photocatalyst (B, C, D, and E) on their oxidation using ZnO@SB, and the mineralization efficiency (F) (Notice 0.2, 0.3, 0.4, and 0.5 g/L ZnO@SB solid dosage).

3.2.2. Mineralization efficiency

To assess the extent of mineralization achieved during the photocatalytic degradation of 4-chlorophenol (4-CL), total organic carbon (TOC) analyses were conducted on treated solutions. This assessment aimed not only to verify the breakdown of the parent compound but also to determine the conversion of residual organic matter into final mineralized products—principally carbon dioxide (CO_2) and water (H_2O)—as well as to detect the persistence or formation of intermediate organic byproducts during oxidation. The experiments employed ZnO@SB at varying dosages (ranging from 0.2 g/L to 0.5 g/L) in systems containing 5 mg/L of 4-CL. TOC measurements were recorded at progressive time intervals to monitor the temporal evolution of mineralization efficiency (Fig. 7F). The results indicated a notable reduction in TOC values over time, confirming the photocatalytic system's efficacy in degrading not only the parent pollutant but also its intermediate transformation products.

Interestingly, a temporal lag was observed between the complete degradation of 4-CL molecules and the full mineralization of the corresponding organic carbon content. While total 4-CL removal was achieved within 40 minutes and 30 minutes using ZnO@SB at dosages of 0.4 g/L and 0.5 g/L, respectively, complete TOC elimination required longer durations—80 minutes and 60 minutes for the same photocatalyst loadings (Fig. 7F). This discrepancy implies that the photocatalytic oxidation process initially yields partially oxidized intermediates, which require additional exposure to reactive oxidative species for further breakdown and final conversion into CO_2 and H_2O. The delayed reduction in TOC, relative to the faster disappearance of the parent compound, highlights the complexity of the degradation pathway and suggests a multistep mechanism. During the initial stages, ZnO@SB

facilitates the rapid oxidative cleavage of 4-CL's aromatic structure, producing less complex but still organic intermediates. These intermediates persist transiently in solution and necessitate additional oxidation steps before full mineralization is realized.

Nevertheless, the eventual complete TOC removal confirms the photocatalyst's ability to drive the reaction to completion, achieving full detoxification and mineralization of 4-CL. This is a crucial consideration for practical applications, as the mere disappearance of the parent molecule does not guarantee the absence of harmful or persistent secondary byproducts. The ability of ZnO@SB to achieve both degradation and mineralization positions it as a promising candidate for advanced wastewater treatment technologies.

3.2.4. Recyclability properties

The reusability of the ZnO@SB photocatalyst was rigorously evaluated through five consecutive photocatalytic cycles (denoted as RN1 to RN5) to assess its durability and operational feasibility for repeated 4-chlorophenol (4-CL) degradation. Following each degradation run, the photocatalyst was recovered via filtration, thoroughly rinsed with distilled water for 15 minutes to remove residual organic and inorganic species, and subsequently dried at 60 °C for 12 hours to ensure complete regeneration before reuse. Photocatalytic experiments were performed under optimal reaction conditions—specifically, a ZnO@SB dosage of 0.5 g/L, reaction volume of 50 mL, pH 8, and a reaction time of 120 minutes (Fig. 8). The experimental results demonstrated that ZnO@SB maintained excellent oxidative performance across all reuse cycles. Complete degradation (100%) of 4-CL at an initial concentration of 5 mg/L was achieved during the first two cycles (RN1 and RN2), while slightly reduced efficiencies of 97.4%, 95.1%, and 90.6% were observed in the subsequent RN3, RN4, and RN5 cycles, respectively (Fig. 8).

These findings underscore the superior regeneration capability and structural stability of ZnO@SB, which outperformed the comparative reference photocatalyst in maintaining degradation efficiency over repeated uses. The modest decline in photocatalytic activity over successive cycles is a common phenomenon in heterogeneous photocatalysis and is primarily attributed to the gradual surface passivation of active sites. This may result from the formation of stable complexes or persistent organic intermediates adsorbed onto the photocatalyst surface, which partially obstruct access to reactive sites. The leachability of Zn

ions after each photocatalytic cycle was evaluated by analyzing the filtrate using inductively coupled plasma–optical emission spectroscopy, confirming a minimal Zn release (< 0.005 mg/L) and demonstrating the excellent structural stability and environmental safety of the ZnO@SB photocatalyst during repeated use. The negligible zinc leaching further corroborated the material's structural robustness and suitability for prolonged use, reducing the risk of secondary contamination in treated water—an essential consideration for environmental compliance and large-scale deployment. Additionally, the comparison between the fresh and used FT-IR spectra shows very minor spectral changes, indicating that the ZnO@SB photocatalyst remains structurally stable after the degradation of 4-chlorophenol (Fig. S4). Only slight variations are observed in the O–H stretching region (≈3420–3450 cm^{-1}) and the H–O–H/organic residue band around ~1635–1640 cm^{-1}, which are attributed to small amounts of adsorbed water or trace reaction intermediates on the surface. All key structural bands—particularly the Si–O–Si/Si–O–Al framework vibration near 1000–1010 cm^{-1} and the Zn–O lattice bands at ≈700, 540, and 470 cm^{-1}—remain unchanged in position and shape. These observations confirm that no structural degradation, dissolution, or chemical transformation of the ZnO@SB composite occurred during the photocatalytic process.

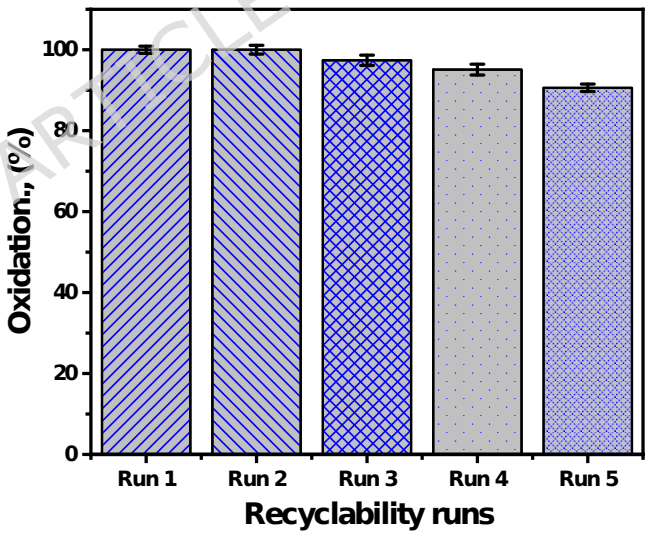

Fig.8. The recyclability properties of ZnO@SB during the oxidation of 4-CL molecules

The sustained high degradation efficiency, even after multiple cycles, highlights the potential of ZnO@SB as a practical and sustainable photocatalyst for industrial wastewater treatment. Its enhanced photocatalytic activity and recyclability can be ascribed to the engineered structural features and surface properties that promote the generation and transfer of reactive species. Furthermore, the gradual efficiency reduction observed over time

aligns with the typical operational behavior of durable photocatalysts subjected to continuous stress, indicating a high tolerance for repeated use without significant performance loss. Overall, ZnO@SB presents a promising solution for the efficient and environmentally responsible removal of recalcitrant organic pollutants such as 4-CL from aqueous systems. Its recyclability, structural integrity, and low environmental impact position it as a strong candidate for integration into advanced oxidation processes (AOPs) in real-world water remediation.

3.2.5. Synergetic properties of oxidation system

The synergistic behavior of carbonaceous bentonite (CB), sulfonated bentonite (S.CB), zinc oxide (ZnO), and their composite (ZnO@SB) was systematically investigated to evaluate their adsorption and photocatalytic performance in the removal of 4-chlorophenol (4-CL). Experiments were conducted under three distinct conditions to distinguish the individual contributions of each material: adsorption in the absence of light, photolysis under visible-light irradiation without any photocatalyst, and photocatalysis under visible light in the presence of the materials. All experiments were carried out under standardized conditions, including a photocatalyst dosage of 0.5 g/L, an initial 4-CL concentration of 20 mg/L, a reaction volume of 50 mL, pH 8, and a total reaction time of 180 minutes (Fig. 9).

In dark conditions, the materials displayed varying adsorption capacities, with removal efficiencies of 11.3% for CB, 27.6% for S.CB, 6.4% for ZnO, and 46.8% for ZnO@SB (Fig. 9). The improved adsorption performance of S.CB over unmodified CB can be attributed to the introduction of sulfonic functional groups during the sulfonation process, which enhance surface polarity and generate additional active sites for pollutant interaction. The significantly higher adsorption efficiency observed for ZnO@SB is indicative of a synergistic enhancement due to the integration of ZnO nanoparticles within the functionalized bentonite matrix. This hybridization likely improves both the surface area and the density of energetically favorable adsorption sites, thereby facilitating the uptake of 4-CL molecules through increased molecular interaction and accessibility.

Control experiments involving photolysis under visible light, in the absence of any photocatalyst, resulted in negligible degradation of 4-CL, with only 0.7% removal observed. This confirms the inherent photostability of the compound and highlights the necessity of a

photocatalyst to initiate degradation under visible light. When the materials were introduced under visible-light irradiation, only ZnO and ZnO@SB exhibited significant photocatalytic activity (Fig. 9). CB and S.CB, while effective adsorbents, showed no meaningful contribution to light-driven degradation. The removal efficiencies under photocatalytic conditions were 28.6% for ZnO and 100% for ZnO@SB (Fig. 9), measured after the establishment of adsorption–desorption equilibrium. These findings clearly demonstrate the substantial improvement in photocatalytic activity achieved through the formation of the ZnO@SB composite.

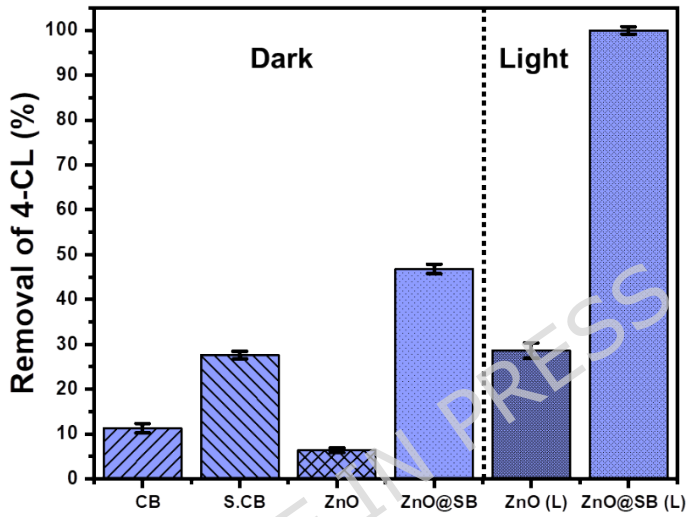

Fig.9. the synergetic effect of the integrated components on the adsorption and photocatalytic performances of ZnO@SB

The enhanced performance of ZnO@SB is ascribed to multiple interrelated mechanistic factors. The sulfonated bentonite framework promotes pre-adsorption of 4-CL molecules near catalytically active ZnO sites, effectively increasing local reactant concentrations. This enhances the likelihood of oxidative degradation once the photocatalytic reaction is initiated. The integration of ZnO further increases the available surface area and the number of photocatalytic sites, while its homogeneous dispersion across the sulfonated matrix prevents agglomeration, ensuring maximal light harvesting and reactive surface exposure. Additionally, the composite structure improves charge separation efficiency by facilitating the migration of photogenerated electrons and holes, thereby suppressing recombination losses. This prolongs the lifetime of reactive charge carriers and promotes the generation of highly oxidative species such as hydroxyl radicals (•OH) and superoxide anions ($O_2^{\bullet -}$), which are crucial for efficient photocatalytic degradation.

The cumulative effects of enhanced adsorption affinity, expanded active surface area, efficient photon utilization, and improved charge carrier dynamics collectively account for the remarkable photocatalytic efficiency of ZnO@SB. These results underscore the advantages of material hybridization in achieving superior performance and demonstrate the potential of ZnO@SB as a robust, cost-effective, and scalable photocatalyst for the degradation of persistent organic pollutants. Its dual-functionality and visible-light responsiveness make it particularly attractive for environmental applications, including the treatment of industrial and pharmaceutical wastewater.

3.2.6. Kinetic behavior and quantum yield evaluation

To elucidate the underlying mechanism of 4-CL oxidation via photocatalysis over the ZnO@SB nanocomposite, a detailed kinetic investigation was conducted using both pseudo-first-order (Eq.1) and pseudo-second-order kinetic (Eq.2) models. The experimental data were fitted to their respective linearized rate expressions, as follows [26]:

$$\ln\frac{C_o}{C_t} = kt \qquad (1)$$

$$\frac{1}{C_t} = \frac{1}{C_0} + k_2 t \qquad (2)$$

Here, C_0 and C_t are the ammonium concentrations at time zero and time t, respectively, and k_1, $k_2$represent the corresponding rate constants for pseudo-first-order and pseudo-second-order kinetics. Analysis of the fitting results revealed that the oxidation of 4-CL consistently followed pseudo-first-order kinetics across all tested initial concentrations and photocatalyst dosages, particularly at specific 4-CL levels (Figure 10A-J; Table 1). This conclusion is supported by higher correlation coefficients and superior linear agreement with the pseudo-first-order model. These findings indicate that the reaction kinetics are primarily influenced by the availability of surface-active oxidizing species rather than by complex adsorption-desorption equilibria or multi-reactant interactions. However, both kinetic models provided insight into different concentration regimes, indicating that multiple parallel oxidation pathways may be operative. This suggests the generation of diverse reactive oxygen species (ROS), such as hydroxyl radicals (•OH) and superoxide anions ($O_2^{\bullet -}$), during photocatalytic irradiation, contributing simultaneously to the degradation process. These

species are known to be strongly dependent on the surface interactions and photogenerated charge carriers of the semiconductor photocatalyst.

The calculated rate constants exhibited a decreasing trend with increasing 4-CL concentrations (Table 1), implying that elevated pollutant loads may hinder photocatalytic performance by reducing the number of available active sites or through radical scavenging, consistent with surface saturation effects. This inhibitory effect has also been linked to competitive adsorption and limited light penetration due to higher turbidity or solute interference. Conversely, increasing the ZnO@SB dosage resulted in a notable enhancement in rate constants, underscoring the role of additional photocatalytic surface area and increased ROS production in accelerating the degradation reaction. These results reinforce that optimal performance is achieved under low-to-moderate pollutant concentrations, where sufficient photocatalytic activity and photon absorption are maintained.

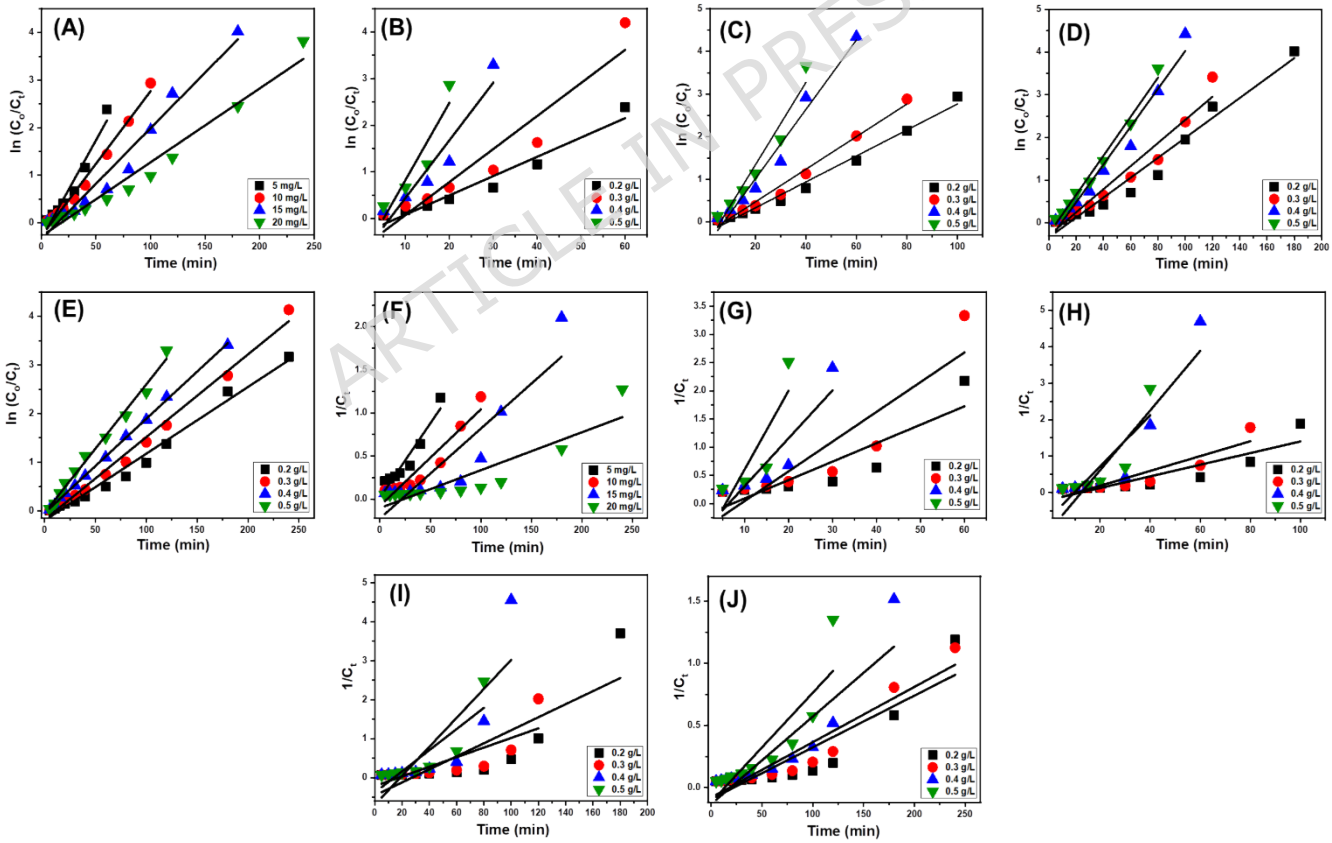

Fig.10. linear fitting of the oxidation results with the First order (A (starting concentration), B (different dosages at 5 mg/L of 4-CL), C (different dosages at 10 mg/L of 4-CL), D (different dosages at 15 mg/L of 4-CL), and E (different dosages at 20 mg/L of 4-CL)) and Second order (F (starting concentration), G (different dosages at 5 mg/L of 4-CL), H (different dosages at 10 mg/L of 4-CL), I (different dosages at 15 mg/L of 4-CL), and J (different dosages at 20 mg/L of 4-CL)) kinetic models

To further quantify the system's photochemical efficiency, the quantum yield (Φ) was assessed. Quantum yield is defined as the ratio of the number of pollutant molecules degraded to the number of incident photons absorbed (Eq. 3), providing a fundamental measure of the efficiency of photon-to-chemical energy conversion [92, 93]. In this study, Φ was calculated via two complementary approaches: a direct molar ratio and a rate constant-based formulation (Eq. 4) [41, 94]:

$$\phi = \frac{\text{Number of 4-CL}}{\text{Number of absorbed photons}} \quad (3)$$

$$\Phi = \frac{K_1}{2.303 \times I_{o,\lambda} \times \varepsilon\lambda \times l} \quad (4)$$

Where k_1 (s^{-1}) is the pseudo-first-order rate constant, $I_{0,\lambda}$ (Einstein·L^{-1}·s^{-1}) is the intensity of incident light at wavelength (λ), ελ (cm^{-1}·M^{-1}) is the molar absorptivity of the system, and ℓ (cm) is the optical path length of the quartz reactor. The derived Φ values exhibited a clear inverse relationship with increasing ammonium concentrations. As pollutant levels rose, Φ decreased markedly, indicating a reduction in the system's photonic efficiency. This can be attributed to multiple inhibitory effects, including enhanced scattering and absorption of incident light by the denser solute matrix, saturation of active sites on the photocatalyst surface, and competitive consumption of ROS by excess ammonium ions. These phenomena collectively reduce the efficiency of photon utilization and charge carrier dynamics, ultimately hindering photocatalytic activity. On the other hand, increasing the ZnO@SB photocatalyst dosage significantly improved Φ, this can be attributed to enhance light absorption, increased number of active sites, and more efficient generation of ROS. The improved interaction between light photons and 4-CL molecules at higher photocatalyst loadings also contributes to enhanced quantum efficiency. These observations are in agreement with the kinetic trends and affirm the critical role of operational parameters in optimizing photocatalytic performance. In summary, the synergistic evaluation of reaction kinetics and quantum yield highlights the high photocatalytic competence of ZnO@SB, particularly under low pollutant concentrations—conditions often encountered in environmental remediation scenarios. These findings underscore the necessity of optimizing key operational variables, such as photocatalyst loading, initial contaminant concentration, and light intensity, to achieve maximal degradation rates and photonic efficiencies in practical applications.

Table 1. The estimated parameters of the kinetic models and the quantum yield efficiency

Conditions	First order model			Second order model			Quantum yield
	R^2	X^2	K_1	R^2	X^2	K_2	
Concentration							
5 mg/L	0.94	0.191	0.0414±0.0	0.90	0.058	0.0172±0.0	7.39×10^{-8}
10 mg/L	0.98	0.118	0.0304±0.0	0.90	0.105	0.0112±0.001	5.42×10^{-8}
15 mg/L	0.96	0.533	0.0233±0.0	0.80	0.693	0.0104±0.0	4.16×10^{-8}
20 mg/L	0.96	0.546	0.0155±0.027	0.78	0.279	0.0043±0.008	2.76×10^{-8}
Dosages at 5 mg/L 4-CL content							
0.2 g/L	0.94	0.191	0.0414±0.0	0.90	0.631	0.0172±0.0	7.39×10^{-8}
0.3 g/L	0.89	0.105	0.0708±0.004	0.78	1.347	0.0527±0.011	1.26×10^{-7}
0.4 g/L	0.88	0.543	0.1237±0.009	0.75	1.598	0.0851±0.023	2.21×10^{-7}
0.5 g/L	0.81	0.489	0.1657±0.022	0.60	1.873	0.1398±0.053	2.96×10^{-7}
Dosages at 10 mg/L 4-CL content							
0.2 g/L	0.98	0.118	0.0304±0.0	0.90	0.105	0.0112±0.001	5.42×10^{-8}
0.3 g/L	0.98	0.112	0.0382±0.001	0.80	0.943	0.0203±0.003	6.82×10^{-8}
0.4 g/L	0.96	0.406	0.0811±0.006	0.81	1.063	0.0818±0.015	1.45×10^{-7}
0.5 g/L	0.94	0.403	0.0966±0.010	0.67	1.462	0.0923±0.020	1.72×10^{-7}
Dosages at 15 mg/L 4-CL content							
0.2 g/L	0.96	0.533	0.0233±0.0	0.80	0.693	0.0104±0.0	4.16×10^{-8}
0.3 g/L	0.95	0.568	0.0270±0.0021	0.62	1.122	0.0233±0.003	4.82×10^{-8}
0.4 g/L	0.97	0.511	0.0443±0.0026	0.65	2.278	0.0371±0.006	7.91×10^{-8}
0.5 g/L	0.98	0.129	0.0457±0.0020	0.71	1.173	0.0412±0.004	8.16×10^{-8}
Dosages at 20 mg/L 4-CL content							
0.2 g/L	0.96	0.546	0.0155±0.027	0.78	0.279	0.0043±0.0081	2.76×10^{-8}
0.3 g/L	0.98	0.164	0.0170±0.031	0.88	0.134	0.0044±0.007	3.03×10^{-8}
0.4 g/L	0.99	0.099	0.0194±0.013	0.79	0.352	0.0070±0.001	3.46×10^{-8}
0.5 g/L	0.98	0.1005	0.0264±0.017	0.75	0.328	0.0088±0.001	4.71×10^{-8}

3.2.7. Suggested mechanism

3.2.7.1. The affected oxidizing species

The reactive species involved in the photocatalytic degradation of 4-chlorophenol (4-CL) using ZnO@SB were examined through selective scavenging experiments. Ethylenediaminetetraacetic acid disodium salt (EDTA-2Na), isopropanol (I-P), and 1,4-benzoquinone (B-Q) were employed as quenchers for photogenerated holes (h^+), hydroxyl radicals (•OH), and superoxide radicals ($O_2^{\bullet -}$), respectively. Each scavenger (1 mM) was introduced into the reaction system containing 0.5 g/L ZnO@SB and 5 mg/L 4-CL at pH 8, and the photocatalytic trials were conducted under visible-light irradiation for 120 minutes. The presence of these scavengers caused distinct reductions in the degradation performance, providing clear insight into the dominant oxidative pathways. The removal efficiency dropped to 16.4% with I-P, 47.2% with B-Q, and 94.8% with EDTA-2Na. The strong inhibitory effect of isopropanol indicates that hydroxyl radicals (•OH) constitute the principal oxidizing species driving the degradation of 4-CL. Meanwhile, the significant reduction observed with benzoquinone demonstrates the important secondary role of superoxide radicals ($O_2^{\bullet -}$). The minimal suppression in the presence of EDTA-2Na suggests that photogenerated holes contribute only marginally to the overall process.

These findings highlight the mechanistic significance of radical pathways in the photocatalytic system. The dominance of •OH reflects highly efficient interfacial charge separation and strong oxidative activity at the ZnO–bentonite interface, while the contribution of $O_2^{\bullet -}$ indicates effective electron transfer and oxygen activation facilitated by the composite structure. The limited role of h^+ further suggests that electron-driven processes are favored, consistent with the enhanced charge mobility afforded by the sulfonated bentonite support. Overall, the scavenging results confirm that the superior performance of ZnO@SB originates from a synergistic radical-mediated mechanism dominated by hydroxyl radicals and supported by superoxide species.

3.2.7.2. General oxidation mechanism and pathway

The photocatalytic degradation of 4-chlorophenol (4-CL) over the ZnO@sulfonated bentonite (ZnO@SB) nanocomposite is governed by a complex sequence of light-induced redox processes, molecular adsorption, generation of reactive oxygen species (ROS), and oxidative transformation of aromatic intermediates (Fig. 11) [95, 96]. Under visible-light irradiation, ZnO acts as the primary photoactive component, absorbing photons with energy equal to or greater than its bandgap and generating electron-hole pairs through excitation of valence band electrons to the conduction band (Eq. 5) [97].

$$ZnO + h\nu \rightarrow e^-_{CB} + h^+_{VB} \quad (5)$$

The photogenerated conduction band electrons are scavenged by dissolved molecular oxygen, producing superoxide anion radicals ($O_2^{\bullet -}$), while valence band holes oxidize hydroxide ions or water molecules to yield hydroxyl radicals ($^{\bullet}OH$) [98]. These fundamental redox reactions can be summarized by Eqs. 6 and 7

$$O_2 + e^- \rightarrow O_2^{\bullet -} \quad (6)$$

$$h^+ + OH^- \rightarrow {\bullet}OH \; ; \; h^+ + H_2O \rightarrow {\bullet}OH + H^+ \quad (7)$$

These ROS species are central to the oxidative degradation mechanism of 4-CL. Prior to oxidation, 4-CL is adsorbed onto the surface of ZnO@SB (Fig. 11) [96]. The sulfonated bentonite component enhances this adsorption through a combination of hydrogen bonding, electrostatic interactions, and acid–base affinities facilitated by its abundant –SO_3H and –OH groups [47, 50]. At a solution pH near 8, 4-CL exists partly in its phenolate anion form, which promotes stronger surface interactions with the polar bentonite structure (Eq. 8) [87, 99]:

$C_6H_4ClOH \rightleftharpoons C_6H_4ClO^- + H^+$ (8)

Following adsorption, the initial ROS-driven transformation involves hydroxylation of the aromatic ring by •OH radicals (Eq. 9). This yields dihydroxylated chlorinated intermediates, such as 4-chlorocatechol, 4-chlorohydroquinone, and chlororesorcinol, depending on the site of radical attack (Fig. 11) [96, 100, 101]. These compounds are more susceptible to subsequent oxidation due to increased electron density and weakened C–Cl bonds:

$C_6H_4ClOH + •OH \rightarrow ClC_6H_3(OH)_2$ (9)

Further oxidative steps lead to dechlorination, where the C–Cl bond is cleaved and chloride ions are released into solution (Eq. 10) [102-105]. The resulting intermediates are non-chlorinated dihydroxybenzenes, such as catechol, hydroquinone, and resorcinol:

$ClC_6H_3(OH)_2 + •OH \rightarrow C_6H_4(OH)_2 + Cl^-$ (10)

The degradation then proceeds via aromatic ring cleavage, initiated by further ROS attack [89, 99]. These reactions produce open-chain dicarboxylic acids, such as muconic acid, maleic acid, and fumaric acid, which are successively oxidized to shorter-chain mono- and dicarboxylic acids including oxalic acid, formic acid, and acetic acid (Eq. 11) (Fig. 11) [96]. These transformations reflect the progressive oxidative fragmentation of the aromatic structure:

$C_6H_4(OH)_2 + ROS \rightarrow (COOH)_2 + CH_3COOH + HCOOH + \ldots$ (11)

Ultimately, the low molecular weight intermediates are mineralized to carbon dioxide and water, achieving complete detoxification of the original compound (Eq. 12) [96]:

$C_nH_mO_x + ROS \rightarrow CO_2 + H_2O + Cl^-$ (12)

The identification of key intermediates—such as chlorocatechols, hydroquinone, and oxalic acid—via chromatographic and spectroscopic analyses in similar systems confirms the validity of this mechanistic pathway. These compounds represent crucial markers for tracking reaction progression and evaluating degradation completeness. Notably, the release of chloride ions can be quantitatively monitored to assess the extent of dechlorination, a critical step toward pollutant detoxification.

The superior efficiency of the ZnO@SB system is not solely due to the photoreactivity of ZnO but is greatly amplified by the synergistic role of the sulfonated bentonite matrix. This

component significantly improves the adsorption capacity of the composite, increasing the local concentration of 4-CL near the photoactive surface. Additionally, its polar and acidic surface functionalities facilitate water activation, enhance ROS generation, and stabilize photogenerated charge carriers by acting as electron acceptors or trap states, thereby suppressing recombination losses. The uniform dispersion of ZnO nanoparticles across the layered bentonite surface also contributes to higher light-harvesting efficiency and improved charge transport.This integrated mechanism demonstrates that ZnO@SB not only enables visible-light-driven activation of oxygen and water but also sustains a cascade of well-coupled redox reactions leading to the complete mineralization of 4-CL. The process is efficient under ambient conditions, requires no sacrificial agents, and proceeds through detoxified intermediates, making it highly suitable for application in advanced oxidation processes for wastewater treatment. The cooperative behavior between semiconductor photoactivation and functionalized support-mediated adsorption and charge control underpins the photocatalyst's high activity and environmental compatibility.

Fig.11. Schematic diagram for the oxidation mechanism and pathway of 4-CL molecules over ZnO@SB photocatalyst. *Chemical structures drawn in ChemDraw Professional v25.0 (Revvity Signals, https://revvitysignals.com/products/chemdraw), then arranged and annotated in Adobe Illustrator v29.8.1 (Adobe Inc.).*

3.2.9. Comparison study

A comprehensive comparison was conducted to contextualize the photocatalytic performance of the synthesized ZnO@SB photocatalyst in the degradation of 4-chlorophenol (4-CL). This assessment integrated the principal operational parameters—initial pollutant concentration, catalyst dosage, irradiation conditions, and reaction duration—and contrasted the activity of ZnO@SB with several state-of-the-art photocatalysts previously reported in the literature (Table 2). The results demonstrate that ZnO@SB exhibits outstanding visible-light-driven degradation efficiency, achieving complete removal of 4-CL within markedly shorter reaction times and with relatively low photocatalyst loading. This rapid and efficient degradation highlights the strong intrinsic activity of the ZnO@SB system and confirms its effectiveness across varying pollutant concentrations. The comparative assessment further reinforces the technical reliability and operational robustness of ZnO@SB. When benchmarking against Au/ZnO, $BiVO_4/WO_3$, g-C_3N_4-based hybrids, and other advanced catalysts, ZnO@SB consistently performs at equal or superior levels under milder conditions. The catalyst's ability to achieve near-quantitative degradation in significantly reduced irradiation times underscores its efficient light harvesting, improved charge separation, and optimized surface interactions.

Table.2. The photocatalytic performance of ZnO@SB during the degradation of 4-CL in comparison with other materials in literature

Catalysts	Dosage	Conc,.	Light source	Degradation performance	References
ZrO_2/g-C_3N_4	60 mg	30 mg/L	300 W Xe lamp	120 min, ca. 90 %	[106]
$BiVO_4/WO_3$	0.125 g/L	25 mg/L	50 W LED lamps	300 min, ca. 97 %	[107]
g- $C_3N_4/Bi_2MoO_6/CeO_2$	30 mg	10 mg/L	300 W Xe lamp	80 min, ca. 99.1 %	[108]
Au/ZnO NRs	-----	10 mg/L	Solar irradiation	300 min, ca. 100 %	[109]
ZnO/gC_3N_4/carbon xerogel	100 mg	10 mg/L	Visible light: 400 W lamp	300 min, ca. 92 %	[110]
$FeTiO_3/TiO_2$	------	6 mg/L	UV	180 min, ca. 75 %	[111]
FeOCl/CDots	1.0 g/L	5 mg/L	Visible light	180 min, ca. 90.1 %	[112]
ZnO/PPy/CNTs	0.5 g/L	10 mg/L	500 W Xe lamp	130 min, ca. 100 %	[113]
Al Fe PILC	0.5 g/L	20 mg/L	Visible light	195 min, ca. 100 %	[114]
ZnO@SB	**0.5 g/L**	**5 mg/L**	**400 W Metal halide lamp**	**30 min, ca. 100 %**	**This study**
ZnO@SB	**0.5 g/L**	**10 mg/L**	**400 W Metal halide lamp**	**60 min, ca. 100 %**	**This study**
ZnO@SB	**0.5 g/L**	**15 mg/L**	**400 W Metal halide lamp**	**100 min, ca. 100 %**	**This study**

ZnO@SB	**0.5 g/L**	**15 mg/L**	**400 W Metal halide lam**	**180 min, ca. 100 %**	**This study**

Beyond its strong photocatalytic performance, ZnO@SB offers several practical and economic advantages. Its fabrication relies on abundant, naturally occurring bentonite, a low-cost precursor that can be readily modified through a simple sulfonation process. Combined with the accessible synthesis route of ZnO nanoparticles, the overall preparation remains straightforward, scalable, and economically favorable. This positions ZnO@SB as a credible alternative to more expensive or synthetically demanding catalysts, particularly for large-scale environmental treatment systems. Overall, the comparison highlights that the exceptional efficiency of ZnO@SB—together with its ease of preparation, stability, and economic viability—makes it a highly promising photocatalyst for real-world wastewater remediation applications.

3.2.8. Health and safety aspects of ZnO@SB photocatalyst

The implementation of photocatalytic materials in water treatment systems must align with global environmental safety standards and human health protection benchmarks (Fig. 12). The integration of ZnO@SB photocatalyst into industrial and municipal water treatment systems necessitates a proactive assessment of occupational safety to ensure the protection of personnel during all stages of the photocatalyst's lifecycle. The immobilization of ZnO nanoparticles onto the sulfonated bentonite support markedly reduces the risk of nanoparticle aerosolization—a critical concern in occupational exposure scenarios involving free nano-ZnO. This structural immobilization minimizes potential inhalation hazards and limits photocatalyst dispersion onto surfaces or into ventilation systems. Furthermore, the composite operates efficiently under mild, ambient conditions (neutral pH, room temperature, and visible light), eliminating the need for hazardous reagents or high-temperature equipment, thereby reducing operator exposure to thermal stress, chemical burns, and phototoxicity. Its regeneration process—limited to simple water rinsing and drying—avoids the use of solvents or caustic agents, thus enabling safe and routine maintenance without requiring extensive personal protective equipment (PPE) or specialized disposal procedures (Fig. 12).

From a human factors engineering perspective, the ZnO@SB system supports a user-centered operational model that enhances safety, usability, and efficiency (Fig. 12). Its

compatibility with low-complexity reactor designs and decentralized treatment infrastructure simplifies training requirements and minimizes the potential for human error during installation, operation, and regeneration. By removing the need for intensive process control, hazardous material handling, or complex instrumentation, the system reduces cognitive load and physical demands on operators, contributing to a safer and more ergonomic work environment. These features align with recognized principles of human-systems integration and occupational ergonomics, promoting sustained workforce performance while maintaining system reliability and process integrity. The photocatalyst's design thus supports compliance not only with environmental and public health standards, but also with occupational safety frameworks such as ISO 45001 and HFE-driven safety protocols.

A critical aspect of environmental and public health safety is the prevention of heavy metal leaching from photocatalytic materials. Elemental analysis of treated effluent revealed that Zn^{2+} release from ZnO@SB remained consistently below 0.005 mg/L across all operating conditions (Fig. 12). This is well under the maximum permissible limits set by the World Health Organization (WHO) for drinking water (3.0 mg/L) and the U.S. EPA (5.0 mg/L), confirming the chemical stability of the composite and its negligible contribution to metal ion contamination. The immobilization of ZnO within the bentonite matrix prevents nanoparticle dissociation, a known concern with free nano-ZnO, which has been associated in literature with oxidative stress, cytotoxicity, and aquatic bioaccumulation.

The photocatalyst exhibited efficient and complete degradation of 4-chlorophenol (4-CL), a toxic compound classified by the U.S. Environmental Protection Agency (EPA) as a priority pollutant and regulated due to its carcinogenicity, endocrine-disrupting potential, and resistance to natural biodegradation. The oxidation pathway involved rapid aromatic hydroxylation, dechlorination, and subsequent ring cleavage, leading to full mineralization into carbon dioxide and water. This was confirmed by TOC measurements, indicating the absence of persistent or harmful intermediates. Importantly, no secondary byproducts such as chlorinated quinones or phenolic acids were detected, thereby fulfilling the detoxification requiremer ient standards.

Fig.12. Schematic diagram for the health and environmental aspects of ZnO@SB as photocatalyst for the oxidation of 4-CL molecules. *Created by the authors in BioRender.com (https://biorender.com).*

Taken together, the ZnO@SB composite satisfies a broad spectrum of environmental and health performance criteria: high pollutant removal efficiency, full mineralization of toxic organics, minimal heavy metal release, safe composition, and reusability without hazardous residues. Its design and behavior are in accordance with the goals outlined in the United Nations Sustainable Development Goals (SDGs), particularly SDG 6 (Clean Water and Sanitation) and SDG 12 (Responsible Consumption and Production). The composite represents a scalable, environmentally compliant solution for the detoxification of phenolic wastewater, offering both regulatory safety and high technical value for industrial and municipal applications.

Conclusions

A novel ZnO-loaded sulfonated carbonaceous bentonite (ZnO@SB) photocatalyst was developed and demonstrated outstanding visible-light-driven performance for the mineralization of 4-chlorophenol (4-CL) in aqueous solutions. The photocatalyst achieved 100% degradation of 4-CL (5 mg/L) within 30 minutes, and complete mineralization (100% TOC removal) within 60 minutes under neutral pH and ambient temperature, using a photocatalyst dosage of 0.5 g/L and a light intensity of 18.7 mW/cm^2. Kinetic modeling revealed pseudo-first-order behavior with a maximum rate constant of k_1 = 0.1657 min^{-1}, while the quantum yield increased significantly from 7.39 × 10^{-8} to 2.96 × 10^{-7} as photocatalyst dosage increased from 0.2 to 0.5 g/L. Mechanistic investigations confirmed the generation of highly reactive oxygen species (•OH, O_2•$^-$), which drove successive

hydroxylation, dechlorination, and aromatic ring cleavage of 4-CL, yielding intermediates such as chlorocatechol and ultimately CO_2 and H_2O. Chloride ion monitoring validated the extent of dechlorination during the photocatalytic process. The ZnO@SB photocatalyst demonstrated excellent reusability, retaining over 90.6% of its initial activity after five successive cycles, with zinc leaching consistently below 0.005 mg/L, well within WHO and EPA safety thresholds.

While these results demonstrate the promising potential of ZnO@SB as an efficient, stable, and environmentally compliant photocatalyst for the removal of chlorinated organic contaminants, the present study was conducted under controlled laboratory conditions using synthetic wastewater. Therefore, further investigations are required to evaluate long-term stability, catalyst durability under continuous operation, and performance in complex real wastewater matrices. Future studies should also explore scale-up feasibility and reactor design optimization to assess the practical applicability of this material in real-world water treatment systems.

Declarations:

AI tools were used during manuscript preparation for language editing and refinement of schematic figures under the authors' supervision, who reviewed all outputs and take full responsibility for the final content

Data availability: The data will be available up on request to corresponding author

Competing interest: The authors declare that they have no known competing or conflicting interests

Funding statement:

This work was supported and funded by the Deanship of Scientific Research at Imam Mohammad Ibn Saud Islamic University (IMSIU) (grant number IMSIU-DDRSP2502)

Authors' contribution:

1. ***Zeinab M. Ahmed:*** Methodology, Visualization, validation, Data curation, Formal analysis, Writing - original draft, Writing – review & editing,
2. **Ahmed A. Allam:** Methodology, Funding, Data curation, Formal analysis, Writing -original draft
3. ***Mohamed I. El-Sayed*:** Supervision, Validation, Writing - original draft, Writing – review & editing
4. ***Ibrahim Mohamed Abd El-Gaied*:** Supervision, Writing – review & editing
5. ***Yasser Salama*:** Methodology, Data curation, Formal analysis, Writing -original draft
6. **Hassan A. Rudayni:** Formal analysis, methodology, Writing - original draft, Writing – review & editing
7. ***Wail Al Zoubi:*** *Validation, Writing - original draft, Writing – review & editing*

8. **Mostafa R. Abukhadra:** Conceptualization, Formal analysis, supervision, Resources, Data curation, Visualization, methodology, validation, Writing - original draft, Writing – review & editing

References

1. *M.H. Dehghani, S. Ahmadi, S. Ghosh, M.S. Khan, A. Othmani, W.A. Khanday, Ö. Gökkuş, C. Osagie, Md. Ahmaruzzaman, S.R. Mishra, E.C. Lima, N.M. Mubarak, R.R. Karri, K. Ansari, Sustainable remediation technologies for removal of pesticides as organic micro-pollutants from water environments: A review, Appl. Surf. Sci. Adv. 19 (2023) 100558.*
2. *P.C. Patel, P.K. Mishra, J. Kashyap, S. Awasthi, Cation doped approach for photodegradation of 4-chlorophenol by highly efficient solar-active NiS photocatalyst: The case of Cu^{2+} doping, J. Photochem. Photobiol. A: Chem. 437 (2022) 114499.*
3. *M. Zarei, Ultrasonic-assisted preparation of ZrO_2/g-C_3N_4 nanocomposites with high visible-light photocatalytic activity for degradation of 4-chlorophenol in water, Water-Energy Nexus 3 (2020) 135–142.*
4. *M. Dai, Z. He, W. Cao, J. Zhang, W. Chen, Q. Jin, W. Que, S. Wang, Rational construction of S-scheme BN/MXene/$ZnIn_2S_4$ heterojunction with interface engineering for efficient photocatalytic hydrogen production and chlorophenols degradation, Sep. Purif. Technol. 309 (2022) 123004.*
5. *E. Taheri, A. Fatehizadeh, S. Hadi, M.M. Amin, M. Khiadani, M. Ghasemian, N. Rafiei, M. Rezakazemi, T.M. Aminabhavi, Mesoporous bimetallic S-doped nanoparticles prepared via hydrothermal method for enhanced photodegradation of 4-chlorophenol, J. Environ. Manage. 349 (2023) 119460.*
6. *Y.M. Hunge, A.A. Yadav, S.-W. Kang, H. Kim, Facile synthesis of multitasking composite of silver nanoparticle with zinc oxide for 4-nitrophenol reduction, photocatalytic hydrogen production, and 4-chlorophenol degradation, J. Alloys Compd. 928 (2022) 167133.*
7. *C. Lopes, J. Restivo, C.A. Orge, M.F.R. Pereira, O.S.G.P. Soares, Catalytic hydrodechlorination of 4-chlorophenol: Role of metal phase supports and reaction pH, J. Water Process Eng. 67 (2024) 106240.*
8. *F. Mumtaz, B. Li, M.R. Al Shehhi, X. Feng, K. Wang, Treatment of phenolic wastewater by hybrid technologies: A review, J. Water Process Eng. 57 (2024) 104695.*
9. *J. Ayach, W. El Malti, L. Duma, J. Lalevée, M. Al Ajami, H. Hamad, A. Hijazi, Conventional versus advanced approaches for heavy-metal removal in wastewater: A filter-based perspective, Polymers 16 (2024) 1959.*
10. *Y. Zhao, C. Chang, H. Ji, Z. Li, Challenges of petroleum-wastewater treatment and trends in advanced technologies, J. Environ. Chem. Eng. 13 (2024) 113767.*
11. *Oyetade, J.A., Machunda, R.L., Hilonga, A. and De Buysser, K., 2025. Development of ternary PANI/GO-Fe3O4@ AgNps nanocomposites for photocatalytic remediation of toxic dye effluent under energy-efficient system. Journal of Molecular Structure, 1324, p.140818.*
12. *Satyam, S. and Patra, S., 2024. Innovations and challenges in adsorption-based wastewater remediation: A comprehensive review. Heliyon, 10(9).*
13. *Nthunya, L.N., Bopape, M.F., Mahlangu, O.T., Mamba, B.B., Van der Bruggen, B., Quist-Jensen, C.A. and Richards, H., 2022. Fouling, performance and cost analysis of membrane-based water desalination technologies: A critical review. Journal of Environmental Management, 301, p.113922.*
14. *He, L., Ma, Y., Lei, X., Zhou, H., Yuan, Y., Du, W., Liu, Z., Miao, R. and Guan, Q., 2024. Degradation of 4-chlorophenol through in situ generation of reactive chlorine species in a Zn2CoOx electrocatalytic system. Journal of Environmental Chemical Engineering, 12(1), p.111911.*
15. *M.Y. Soomro, A. Balouch, E. Alveroglu, R. Larik, K. Shah, S.A. Chang, Fe/Ni bimetallic magnetic nano-alloy as an efficient photo-Fenton-like catalyst for phenol degradation, Environ. Pollut. 360 (2024) 124635.*
16. *Patil, D.J. and Grewal, H.S., 2025. Comparative study of heterogeneous activation of H2O2 and peroxymonosulfate over nanoporous ZnFe2O4 for dye degradation via batch and continuous-flow channel approach. Journal of Water Process Engineering, 75, p.108007.*
17. *V.A. Naik, V.A. Thakur, Fe_3O_4@rGO@CdS/Bi_2S_3 magnetic nanocomposite for photo-Fenton dye degradation and Cr(VI) reduction under sunlight, Inorg. Chem. Commun. 160 (2024) 111962.*

18. Oyetade, J.A., Van Hulle, S.W., Machunda, R.L. and Hilonga, A., 2024. Development of photocatalytic semiconductors and nanocomposites with excellent optoelectronic and electrochemical properties for dye effluent remediation-A review. Materials Science in Semiconductor Processing, 184, p.108821.
19. Zhang, Y., Cui, K., Liu, X., Cui, M., Chen, X., Tang, Y., Li, H. and Wang, K., 2024. Important role of carbon doping in photocatalytic peroxymonosulfate activation of carbon nitride for efficient 4-Chlorophenol degradation. Chemical Engineering Journal, 493, p.152482.
20. Patil, D.J., Kumar, R. and Grewal, H.S., 2024. Multifunctional smart engineering nano magnetic materials with ultrahigh synergetic adsorption-photocatalytic performance. Surfaces and Interfaces, 46, p.104106..
21. W. Zeng, Y. Luo, C. Wang, Z. Liu, M. Xue, X. Xie, Recent advances in adsorption and photoreduction of Cr(VI): A review, Environ. Pollut. Bioavailab. 37 (2025) 2493057.
22. de Moraes, N.P., de Campos Sanmartin, M.B., da Silva Rocha, R., de Siervo, A., de Vasconcelos Lanza, M.R., Reddy, D.A., Yu, L. and Rodrigues, L.A., 2024. ZnO/CeO2/carbon xerogel composites with direct Z-scheme heterojunctions: Enhancing photocatalytic remediation of 4-chlorophenol under visible light. Journal of Rare Earths, 42(2), pp.314-322.
23. Wang, Y., Wong, N.H., Sunarso, J., Guo, R., Zhu, C., Liu, M., Chen, G., Dai, G. and Shen, Q., 2025. Fabrication of core-shell shaped heterojunction Bi2MoO6/In2O3 nanofibers as a highly efficient photocatalyst toward degradation of 4-chlorophenol. Journal of Water Process Engineering, 69, p.106702.
24. S. Ghanbari, A. Fatehizadeh, M. Khiadani, E. Taheri, H.M.N. Iqbal, UV/Cl_2/Br photolysis followed by adsorption for dye-laden textile wastewater, Environ. Sci. Pollut. Res. 29 (2022) 39400–39409.
25. Md. Ahmaruzzaman, S.R. Mishra, V. Gadore, G. Yadav, S. Roy, B. Bhattacharjee, A. Bhuyan, B. Hazarika, J. Darabdhara, K. Kumari, Phenolic compounds in water: Toxicity, sources and sustainable removal solutions, J. Environ. Chem. Eng. 12 (2024) 112964.
26. X. Yang, J. Wang, A.M. El-Sherbeeny, A.A. AlHammadi, W.-H. Park, M.R. Abukhadra, Adsorption and oxidation activity of ZnO/quartz core-shell for ibuprofen decontamination, Chem. Eng. J. 431 (2021) 134312.
27. M.K. Zamisa, T.W. Seadira, S.J. Baloyi, Catalytic wet-air oxidation with pillared clay catalysts for phenol remediation, Environ. Pollut. 361 (2024) 124842.
28. Zaki, R.M., Jusoh, R., Chanakaewsomboon, I. and Setiabudi, H.D., 2024. Recent advances in metal oxide photocatalysts for photocatalytic degradation of organic pollutants: A review on photocatalysts modification strategies. Materials Today: Proceedings, 107, pp.59-67.
29. Ma, Y., Duan, Y., Su, H., Li, Y., Chen, Z. and Li, J., 2025. Status and challenges of photocatalysis in environmental applications: Photocatalyst deactivation. Nano Research, 18(9).
30. A. Nawaz, A. Farhan, F. Maqbool, H. Ahmad, W. Qayyum, E. Ghazy, A. Rahdar, A.M. Díez-Pascual, S. Fathi-karkan, Zinc oxide nanoparticles: Pathways to micropollutant adsorption, dye removal, and antibacterial actions—A study of mechanisms, challenges, and future prospects, J. Mol. Struct. 1312 (2024) 138545.
31. J. Liu, H. Wang, H. Wu, Y. Yang, C. Wang, Q. Wang, B. Jia, J. Zheng, Research progress of zinc oxide-based heterojunction photocatalysts, J. Mater. Chem. A (2024) (in press).
32. O.H. Aremu, C.O. Akintayo, E.B. Naidoo, S.M. Nelana, O.S. Ayanda, Synthesis and applications of nano-sized zinc oxide in wastewater treatment: A review, Int. J. Environ. Sci. Technol. (2021) 1–20.
33. E. Zabihi, Z. Arab-Bafrani, S.M. Hoseini, E. Mousavi, A. Babaei, M. Khalili, M.M. Hashemi, N. Javid, Fabrication of nano-decorated ZnO-fibrillar chitosan exhibiting a superior performance as a promising replacement for conventional ZnO, Carbohydr. Polym. 274 (2021) 118639.
34. M. Dimitropoulos, C.A. Aggelopoulos, L. Sygellou, S.T. Tsantis, P.G. Koutsoukos, S.N. Yannopoulos, Unveiling the photocorrosion mechanism of zinc oxide photocatalyst: Interplay between surface corrosion and regeneration, J. Environ. Chem. Eng. 12 (2024) 112102.
35. N.O. Etafo, M.O. Bamidele, A. Bamisaye, Y.A. Alli, Revolutionizing photocatalysis: Unveiling efficient alternatives to titanium(IV) oxide and zinc oxide for comprehensive environmental remediation, J. Water Process Eng. 62 (2024) 105369.

36. A.M. Saad, M.R. Abukhadra, S.A.K. Ahmed, A.M. Elzanaty, A.H. Mady, M.A. Betiha, J.J. Shim, A.M. Rabie, Photocatalytic degradation of malachite green dye using chitosan-supported ZnO and Ce–ZnO nano-flowers under visible light, J. Environ. Manage. 258 (2020) 110043.
37. A. Baig, M. Siddique, S. Panchal, A review of visible-light-active zinc oxide photocatalysts for environmental application, Catalysts 15 (2025) 100.
38. S. Abou Zeid, Y. Leprince-Wang, Advancements in ZnO-based photocatalysts for water treatment: A comprehensive review, Crystals 14 (2024) 611.
39. S.A. Ansari, Development and photocatalytic performance of spherical shape zinc oxide nanoparticles for environmental remediation, J. Nanoelectron. Optoelectron. 20 (2025) 101–105.
40. K. Rabiei, Recent application of clay-based heterogeneous catalyst in organic reactions, J. Inorg. Organomet. Polym. Mater. (2025) 1–22.
41. S.I. Othman, H.E. Alfassam, H.A. Alqhtani, M.H. Shemy, A.A. Allam, M.R. Abukhadra, Characterization of green ZnO-supported curcumin intercalated bentonite (ZnO@CU/BEN) as environmental catalysts for effective oxidation of 5-fluorouracil residuals: Pathway and toxicity, J. Inorg. Organomet. Polym. Mater. 34 (2024) 4116–4132.
42. B. Zhang, W. Zhu, R. Hou, Y. Yue, J. Feng, A. Ishag, X. Wang, Y. Qin, Y. Sun, Recent advances of application of bentonite-based composites in environmental remediation, J. Environ. Manage. 362 (2024) 121341.
43. S. Arabmofrad, S.M. Jafari, G. Lazzara, A.M. Ziaiifar, H. Shahiri Tabarestani, G. Bahlakeh, G. Cavallaro, M.M. Calvino, M. Nasiri Sarvi, Preparation and characterization of surface-modified montmorillonite by cationic surfactants for adsorption purposes, J. Therm. Anal. Calorim. 148 (2023) 13803–13814.
44. M. Wasim, F. Shi, J. Liu, H. Zhang, K. Zhu, Z. Tian, Synthesis and characterization of curcumin/MMT-clay-treated bacterial cellulose as an antistatic and ultraviolet-resistive bioscaffold, J. Polym. Res. 29 (2022) 1–18.
45. L. Tong, T. Liang, Y. Tian, Q. Zhang, Y. Pan, Research progress on treatment of mine wastewater by bentonite composite, Arab. J. Geosci. 15 (2022) 99 (Article ID).
46. F.M. Dardir, A.S. Mohamed, M.R. Abukhadra, E.A. Ahmed, M.F. Soliman, Cosmetic and pharmaceutical qualifications of Egyptian bentonite and its suitability as drug carrier for Praziquantel drug, Eur. J. Pharm. Sci. 115 (2018) 320–329.
47. W.A. Hassan, E.A. Ahmed, M.A. Moneim, M.S. Shaban, A.M. El-Sherbeeny, N. Siddiqui, J.J. Shim, M.R. Abukhadra, Sulfonation of natural carbonaceous bentonite as a low-cost acidic catalyst for effective transesterification of used sunflower oil into diesel, statistical modeling and kinetic properties, ACS Omega 6 (2021) 31260–31271.
48. Z. Kang, Y. Zhao, D. Yang, Review of oil shale in-situ conversion technology, Appl. Energy 269 (2020) 115121.
49. A. Sobhy, A. Yehia, F.E. Hosiny, S.S. Ibrahim, R. Amin, Application of statistical analysis for optimizing of column flotation with pine oil for oil shale cleaning, Int. J. Coal Prep. Util. 42 (2022) 2285–2298.
50. Refaai, M.G., Rudayni, H.A., Allam, A.A., Abukhadra, M.R. and Wahed, M.S.A., 2025. Photocatalytic oxidation of ammonia using copper-mediated phosphotungstic acid intercalated sulfonated bentonite for sustainable eutrophication control: A case study from Lake Qarun. Environmental Research, p.122351.
51. A.H. Jawad, A.S. Abdulhameed, M.M. Hanafiah, Z.A. ALOthman, M.R. Khan, S.N. Surip, Numerical desirability function for adsorption of methylene blue dye by sulfonated pomegranate peel biochar: Modeling, kinetic, isotherm, thermodynamic, and mechanism study, Korean J. Chem. Eng. 38 (2021) 1499–1509.
52. Y. Genel, İ. Genel, C. Saka, Facile preparation of sulfonated carbon particles with pomegranate peels as adsorbent for enhanced methylene blue adsorption from aqueous solutions, Biomass Convers. Biorefin. 14 (2024) 30693–30705.
53. S. Sripada, J.R. Kastner, Catalytic esterification using solid acid carbon catalysts synthesized by sustainable hydrothermal and plasma sulfonation techniques, Ind. Eng. Chem. Res. 61 (2022) 3928–3940.
54. V. Aniya, A. Kumari, D. De, D. Vidya, V. Swapna, P.K. Thella, B. Satyavathi, Translation of lignocellulosic waste to mesoporous solid acid catalyst and its efficacy in esterification of volatile fatty acid, Microporous Mesoporous Mater. 264 (2018) 198–207.

55. N.M. Alsebaii, X. Sun, M.A. Salam, M.R. Abukhadra, Tailoring the activity of sulfonated coal catalyst during the sonication and infrared-induced transesterification of castor (Ricinus communis) oil: Synergetic, optimization, kinetics, and CI engine assessment, Ind. Crops Prod. 210 (2024) 118174.
56. Bayram, H., Ustunisik, G., Önal, M. and Sarıkaya, Y., 2021. Optimization of bleaching power by sulfuric acid activation of bentonite. Clay minerals, 56(2), pp.148-155.
57. Dhar, A.K., Himu, H.A., Bhattacharjee, M., Mostufa, M.G. and Parvin, F., 2023. Insights on applications of bentonite clays for the removal of dyes and heavy metals from wastewater: a review. Environmental Science and Pollution Research, 30(3), pp.5440-5474.
58. Mclaren, A., Valdes-Solis, T., Li, G. and Tsang, S.C., 2009. Shape and size effects of ZnO nanocrystals on photocatalytic activity. Journal of the American Chemical Society, 131(35), pp.12540-12541.
59. Huang, M., Lian, J., Si, R., Wang, L., Pan, X. and Liu, P., 2022. Spatial separation of electrons and holes among ZnO polar {0001} and {1010} facets for enhanced photocatalytic performance. ACS omega, 7(30), pp.26844-26852.
60. Isaacs, M.A., Robinson, N., Barbero, B., Durndell, L.J., Manayil, J.C., Parlett, C.M., D'Agostino, C., Wilson, K. and Lee, A.F., 2019. Unravelling mass transport in hierarchically porous catalysts. Journal of Materials Chemistry A, 7(19), pp.11814-11825.
61. Liu, B., Bie, C., Zhang, Y., Wang, L., Li, Y. and Yu, J., 2021. Hierarchically porous ZnO/g-C3N4 S-scheme heterojunction photocatalyst for efficient H2O2 production. Langmuir, 37(48), pp.14114-14124.
62. S.I. Akinfalabi, U. Rashid, R. Yunus, Y.H. Taufiq-Yap, Synthesis of biodiesel from palm fatty acid distillate using sulfonated palm seed cake catalyst, Renewable Energy 111 (2017) 611–619.
63. M.A. Farabi, M.L. Ibrahim, U. Rashid, Y.H. Taufiq-Yap, Esterification of palm fatty acid distillate using sulfonated carbon-based catalyst derived from palm kernel shell and bamboo, Energy Convers. Manage. 181 (2019) 562–570.
64. L.J. Konwar, P. Mäkelä-Arvela, J.P. Mikkola, SO_3H-containing functional carbon materials: Synthesis, structure, and acid catalysis, Chem. Rev. 119 (2019) 11576–11630.
65. Z. Zailan, M. Tahir, M. Jusoh, Z.Y. Zakaria, A review of sulfonic group-bearing porous carbon catalyst for biodiesel production, Renewable Energy 175 (2021) 430–452.
66. W. Mateo, H. Lei, E. Villota, M. Qian, Y. Zhao, E. Huo, et al., One-step synthesis of biomass-based sulfonated carbon catalyst by direct carbonization-sulfonation for organosolv delignification, Bioresour. Technol. 319 (2021) 124194.
67. M.A. Quintana, R.R. Solís, G. Blázquez, M. Calero, M.J. Munoz-Batista, Sulfonic grafted graphitic-like carbon nitride for the improved photocatalytic production of benzaldehyde in water, Appl. Surf. Sci. 656 (2024) 159717.
68. F.H. Mustafa, H.A.A. Attia, R. Yahya, R.F. Elshaarawy, N. Hassan, Cellulose microfibrils-embedded sulfonated polyethersulfone for efficient Zn^{2+} ion removal from aqueous effluents, Chem. Eng. Res. Des. 186 (2022) 374–386.
69. K. Singh, S. Yadav, Biosynthesis of a range of ZnO nanoparticles utilising Salvia hispanica L. seed extract and evaluation of their bioactivity, Sci. Rep. 15 (2025) 4043.
70. M.A. Hessien, R.M. Khattab, H.E.H. Sadek, Synthesis and characterization of ZnO, Mn_3O_4, and $ZnMn_2O_4$ spinel by a new chelation-precipitation method: Magnetic and antimicrobial properties, J. Inorg. Organomet. Polym. Mater. (2024) 1–20.
71. P. Vassileva, I. Uzunov, T. Popova, D. Voykova, I. Avramova, D. Mehandjiev, Biochars as a solution for silver removal and antimicrobial activity in aqueous systems, Appl. Sci. 15 (2025) 2796.
72. B. Mekonnen, Synthesis and characterization of microporous materials: Towards a versatile adsorbent and a simple model material for the study of adsorption-induced deformation in microporous media, Ph.D. thesis, Université de Pau et des Pays de l'Adour, 2025.
73. N. Hijazi, A. Bavykina, I. Yarulina, T. Shoinkhorova, E.V. Ramos-Fernandez, J. Gascon, Chemical engineering of zeolites: Alleviating transport limitations through hierarchical design and shaping, Chem. Soc. Rev. (2025) (in press).

74. Raha, S. and Ahmaruzzaman, M., 2022. ZnO nanostructured materials and their potential applications: progress, challenges and perspectives. Nanoscale advances, 4(8), pp.1868-1925.
75. Rahimzadeh, H., Tabatabaei, M., Aghbashlo, M., Panahi, H.K.S., Rashidi, A., Goli, S.A.H., Mostafaei, M., Ardjmand, M. and Nizami, A.S., 2018. Potential of acid-activated bentonite and SO3H-functionalized MWCNTs for biodiesel production from residual olive oil under biorefinery scheme. Frontiers in Energy Research, 6, p.137.
76. Sasikala, S.P., Nibila, T.A., Babitha, K.B., Mohamed, A.A.P. and Solaiappan, A., 2019. Competitive photo-degradation performance of ZnO modified bentonite clay in water containing both organic and inorganic contaminants. Sustainable Environment Research, 29(1), p.1.
77. Alshabanat, M., El-Saeid, M.H., Almuqati, N.S., Alshuhri, S.A., Alqarni, A.A., Albugami, T.M., Almansour, M., Albusayr, R., Alshatri, W. and Almarwan, D., 2025. Preparation and characterization of zno/bentonite nanocomposites for enhanced photocatalytic degradation of pesticides in contaminated water. Scientific Reports, 15(1), p.23816.
78. Zyoud, A.H., Zubi, A., Zyoud, S.H., Hilal, M.H., Zyoud, S., Qamhieh, N., Hajamohideen, A. and Hilal, H.S., 2019. Kaolin-supported ZnO nanoparticle catalysts in self-sensitized tetracycline photodegradation: Zero-point charge and pH effects. Applied Clay Science, 182, p.105294.
79. Aadnan, I., Zegaoui, O., El Mragui, A. and Esteves da Silva, J.C.G., 2021. Physicochemical and photocatalytic properties under visible light of ZnO-Bentonite/Chitosan hybrid-biocompositefor water remediation. Nanomaterials, 12(1), p.102.
80. Gebrye, A.B., Mehari, B. and Atlabachew, M., 2025. Photocatalytic performance of ZnO immobilized on bentonite for catalytic degradation of malachite green under sunlight irradiation. Hybrid Advances, p.100542.
81. Priatna, S.J., Yuliana, A., Melwita, E., Arsyad, F.S. and Mohadi, R., 2024. Removal of methyl orange in aqueous medium using ZnO/bentonite as semiconductor by photocatalytic process. Science and Technology Indonesia, 9(3), pp.539-545.
82. Wang, J., Wang, Z., Huang, B., Ma, Y., Liu, Y., Qin, X., Zhang, X. and Dai, Y., 2012. Oxygen vacancy induced band-gap narrowing and enhanced visible light photocatalytic activity of ZnO. ACS applied materials & interfaces, 4(8), pp.4024-4030.
83. Julita, M., Shiddiq, M. and Khair, M., 2022. Determination of band gap energy of ZnO/Au nanoparticles resulting in laser ablation in liquid. Indonesian Journal of Chemical Research, 10(2), pp.83-87.
84. de Mattos Amadio, T., Hotza, D., Neto, J.B.R., Blosi, M., Costa, A.L. and Dondi, M., 2017. Bentonites functionalized by impregnation with TiO2, Ag, Pd and Au nanoparticles. Applied Clay Science, 146, pp.1-6.
85. Li, X., Simon, U., Bekheet, M.F. and Gurlo, A., 2022. Mineral-supported photocatalysts: a review of materials, mechanisms and environmental applications. Energies, 15(15), p.5607.
86. Y. Gao, D. He, L. Wu, Z. Wang, Y. Yao, Z.-H. Huang, H. Yang, M.-X. Wang, Porous and ultrafine nitrogen-doped carbon nanofibers from bacterial cellulose with superior adsorption capacity for adsorption removal of low-concentration 4-chlorophenol, Chem. Eng. J. 420 (2020) 127411.
87. A.M. Farhan, E.S. Khaled, A.A. Abdel-Khalek, B. Salah, W. Al Zoubi, M.R. Abukhadra, Characterization and statistical physics modeling of two coal hybridized nanostructures with two forms of polyaniline (nanofibers hydrogel and nanorods) as adsorbents for toxic 4-chlorophenol, J. Inorg. Organomet. Polym. Mater. (2025) 1–23.
88. S. Hadi, E. Taheri, M.M. Amin, A. Fatehizadeh, T.M. Aminabhavi, Advanced oxidation of 4-chlorophenol via combined pulsed light and sulfate radicals methods: Effect of co-existing anions, J. Environ. Manage. 291 (2021) 112595.
89. R.R. Abdullah, K.M. Shabeed, A.B. Alzubaydi, Q.F. Alsalhy, Novel photocatalytic polyether sulphone ultrafiltration membrane reinforced with oxygen-deficient tungsten oxide ($WO_{2.89}$) for Congo red dye removal, Chem. Eng. Res. Des. 177 (2022) 526–540.
90. C. Wang, R. Sun, R. Huang, Y. Cao, A novel strategy for enhancing heterogeneous Fenton degradation of dye wastewater using natural pyrite: Kinetics and mechanism, Chemosphere 272 (2021) (Article ID).

91. M.A. Salam, M.R. AbuKhadra, A.S. Mohamed, Effective oxidation of methyl parathion pesticide in water over recycled glass-based MCM-41 decorated by green Co_3O_4 nanoparticles, Environ. Pollut. 259 (2020) 113874.
92. M.V. Martin, O.M. Alfano, M.L. Satuf, Cerium-doped TiO_2 thin films: Assessment of radiation absorption properties and photocatalytic reaction efficiencies in a microreactor, J. Environ. Chem. Eng. 7 (2019) 103478.
93. S. Cao, L. Piao, Considerations for a more accurate evaluation method for photocatalytic water splitting, Angew. Chem. Int. Ed. 59 (2020) 18312–18320.
94. A. Huda, R. Ichwani, C.T. Handoko, M.D. Bustan, B. Yudono, F. Gulo, Comparative photocatalytic performances towards acid yellow 17 and direct blue 71 degradation using Sn_3O_4 flower-like structure, J. Phys. Conf. Ser. 1282 (2019) 012097.
95. A. Zada, M. Khan, M.A. Khan, Q. Khan, A. Habibi-Yangjeh, A. Dang, M. Maqbool, Review on the hazardous applications and photodegradation mechanisms of chlorophenols over different photocatalysts, Environ. Res. 195 (2021) 110742.
96. D. Mostafa, M.D. Alqahtani, N. Shehata, M.N.B. Jumah, N.M. Alotaibi, N.A. Alenazi, H.A. Rudayni, A.A. Allam, M.R. Abukhadra, Insight into the impact of calcination on the catalytic performance of synthetic hematite nano-rods during the photo-Fenton oxidation of 4-chlorophenol toxic residuals, Surf. Interfaces (2025) 105970.
97. A. Baig, M. Siddique, S. Panchal, A review of visible-light-active zinc oxide photocatalysts for environmental application, Catalysts 15 (2025) 100.
98. G. Rangarajan, A. Jayaseelan, R. Farnood, Photocatalytic reactive oxygen species generation and their mechanisms of action in pollutant removal with biochar-supported photocatalysts: A review, J. Cleaner Prod. 346 (2022) 131155.
99. J.R. Domínguez, C.J. Durán-Valle, G. Mateos-García, Synthesis and characterisation of acid/basic modified adsorbents: Application for chlorophenols removal, Environ. Res. 207 (2022) 112187.
100. Q. Zhuo, J. Lu, J. Niu, J.C. Crittenden, G. Yu, S. Wang, B. Yang, Z. Chen, Electrocatalytic oxidation processes for treatment of halogenated organic pollutants in aqueous solution: A critical review, ACS ES&T Eng. 2 (2022) 1756–1775.
101. X. Liu, L. Zhang, Q. Zhang, M. Li, Z. Zhao, B. Lin, J. Peng, H. Shen, Q. He, Fenton-like system of UV/glucose-oxidase@kaolin coupled with organic green rust: UV-enhanced enzyme activity and the mechanism of UV synergistic degradation of photosensitive pollutants, Environ. Res. 247 (2024) 118257.
102. K. Yang, I.M. Abu-Reesh, Z. He, Degradation of 4-chlorophenol through cooperative reductive and oxidative processes in an electrochemical system, J. Hazard. Mater. 442 (2023) 130126.
103. H. Mun, D. Wang, J. Zheng, S. Ahmad, M. Ri, C. Ri, J. Tang, Complete 2,4,6-trichlorophenol degradation by anaerobic sludge acclimated with 4-chlorophenol: Synergetic effect of nZVI@BMPC and sodium lactate as an external nutrient, J. Hazard. Mater. 476 (2024) 135063.
104. P. Veerakumar, A. Sangili, S.M. Chen, R.S. Kumar, G. Arivalagan, M.J. Firdhouse, K.S. Hameed, S. Sivakumar, Photocatalytic degradation of phenolic pollutants over palladium-tungsten trioxide nanocomposite, Chem. Eng. J. 489 (2024) 151127.
105. M. Lei, Q. Gao, K. Zhou, P. Gogoi, J. Liu, J. Wang, H. Song, S. Wang, X. Liu, Catalytic degradation and mineralization mechanism of 4-chlorophenol oxidized by phosphomolybdic acid/H_2O_2, Sep. Purif. Technol. 257 (2021) 117933.
106. M. Zarei, Ultrasonic-assisted preparation of ZrO2/g-C3N4 nanocomposites with high visible-light photocatalytic activity for degradation of 4-chlorophenol in water, Water-Energy Nexus 3 (2020) 135–142.
107. A. Dehdar, G. Asgari, M. Leili, T. Madrakian, A. Seid-Mohammadi, Step-scheme BiVO4/WO3 heterojunction photocatalyst under visible LED light irradiation removing 4-chlorophenol in aqueous solutions, Journal of Environmental Management 297 (2021) 113338.
108. Q. Gao, Z. Wang, J. Li, B. Liu, C. Liu, Facile synthesis of ternary dual Z−scheme g−C3N4/Bi2MoO6/CeO2 photocatalyst with enhanced 4–chlorophenol removal: Degradation pathways and mechanism, Environmental Pollution 315 (2022) 120436

109. Z. Al-Sharji, J. Al-Sabahi, H.H. Kyaw, M.T.Z. Myint, M. Al-Abri, Plasmon enhanced photocatalytic degradation of 4-chlorophenol using zinc oxide nanorods decorated with gold nanoparticles as supported catalysts under natural sunlight, Chemical Engineering and Processing - Process Intensification 188 (2023) 109369

110. J.G.M. De Sousa, T.V.C. Da Silva, N.P. De Moraes, M.L.C.P. Da Silva, R. Da Silva Rocha, R. Landers, L.A. Rodrigues, Visible light-driven ZnO/g-C3N4/carbon xerogel ternary photocatalyst with enhanced activity for 4-chlorophenol degradation, Materials Chemistry and Physics 256 (2020) 123651

111. Y. Ma, J. Chen, Y. Wang, Y. Zhao, G. Zhang, T. Sun, Synthesis of FeTiO3/TiO2 composites by a cross-linking method for enhanced photocatalytic degradation of 4-chlorophenol and dyes, Research on Chemical Intermediates 47 (2020) 997–1007. https://doi.org/10.1007/s11164-020-04312-7.

112. J. Zhang, G. Zhang, Q. Ji, H. Lan, J. Qu, H. Liu, Carbon nanodot-modified FeOCl for photo-assisted Fenton reaction featuring synergistic in-situ H2O2 production and activation, Applied Catalysis B Environment and Energy 266 (2020) 118665.

113. H. Xing, C. An, L. Wu, Y. Xu, Fabrication of ZnO/Polypyrrole/Carbon Nanotube Nanocomposite and its Application for Removal of 4-Chlorophenol from Wastewater, International Journal of Electrochemical Science 17 (2022) 220510.

114. C. Catrinescu, D. Arsene, P. Apopei, C. Teodosiu, Degradation of 4-chlorophenol from wastewater through heterogeneous Fenton and photo-Fenton process, catalyzed by Al–Fe PILC, Applied Clay Science 58 (2012) 96–101.